Structural and Multidisciplinary Optimization manuscript No.
(will be inserted by the editor)

High-Fidelity Aerostructural Optimization with Integrated Geometry Parameterization and Mesh Movement

Zimi J. Zhang · Shahriar Khosravi · David W. Zingg

Received: date / Accepted: date

Abstract This paper extends an integrated geometry parameterization and mesh movement strategy for aerodynamic shape optimization to high-fidelity aerostructural optimization based on steady analysis. This approach provides an analytical geometry representation while enabling efficient mesh movement even for very large shape changes, thus facilitating efficient and robust aerostructural optimization. The geometry parameterization methodology uses B-spline surface patches to describe the undeflected design and flying shapes with a compact yet flexible set of parameters. The geometries represented are therefore independent of the mesh used for the flow analysis, which is an important advantage to this approach. The geometry parameterization is integrated with an efficient and robust grid movement algorithm which operates on a set of B-spline volumes that parameterize and control the flow grid. A simple technique is introduced to translate the shape changes described by the geometry parameterization to the internal structure. A three-field formulation of the discrete aerostructural residual is adopted, coupling the mesh movement equations with the discretized three-dimensional inviscid flow equations, as well as a linear structural analysis. Gradients needed for optimization are computed with a three-field coupled adjoint approach. Capabilities of the framework are demonstrated via a number of applications involving substantial geometric changes.

Keywords Multidisciplinary optimization · Aerostructural optimization · Computational fluid dynamics · Aerodynamics · Geometry parameterization · Mesh movement · Coupled adjoint

Nomenclature

AoA	Angle of attack
$\mathbf{B}$	Coordinates of a single control point
$\mathbf{b}$	Vector of control point coordinates
$\mathbf{b}_J$	$\mathbf{b}$ for the jig shape
$\mathbf{b}_\Delta$	$\mathbf{b}$ for the deflected geometry
$\mathbf{b}_s$	Coordinates of surface control points
$\mathbf{b}_{sJ}$	$\mathbf{b}_s$ for the jig shape
$\mathbf{b}_{s\Delta}$	$\mathbf{b}_s$ for the deflected geometry
$\mathscr{C}_{\mathrm{eq}}, \mathscr{C}_{\mathrm{in}}$	Equality and inequality constraint
D	Inviscid drag of the wing
D_0	Initial inviscid drag of the wing
$\mathbf{f}_A$	Aerodynamic surface traction
$\mathbf{f}_M$	Force vector in the mesh equations
$\mathbf{f}_{MJ}$	$\mathbf{f}_M$ for the jig shape
$\mathbf{f}_{M\Delta}$	$\mathbf{f}_M$ for the deflected geometry
$\mathbf{f}_S$	Force vector in the structural equations
FoS	Factor of safety
$\mathbf{G}$	Vector containing all nodes on the flow grid
$\mathbf{G}_{sJ}$	Coordinates of surface grid nodes on the jig shape
$\tilde{\mathbf{G}}_{s\Delta}$	Displaced surface coordinates as described by the displacement transfer
$\mathscr{J}$	Objective function
$\mathscr{J}_A$	Aerodynamic functional
$\mathscr{J}_S$	Structural functional
$\mathbf{K}_M$	Stiffness matrix for the mesh equations

This work was previously presented under the title “High-Fidelity Aerostructural Optimization with Integrated Geometry Parameterization and Mesh Movement” at the 56th AIAA/ASCE/AHS/ASC Structures, Structural Dynamics, and Materials Conference, Kissimmee, FL, January 2015.

Zimi J. Zhang
University of Toronto Institute for Aerospace Studies, Toronto, ON, CA, M3H 5T6
E-mail: jenmyzm.zhang@utoronto.ca

Shahriar Khosravi
University of Toronto Institute for Aerospace Studies

David W. Zingg
University of Toronto Institute for Aerospace Studies

$\mathbf{K}_{MJ}$	$\mathbf{K}_M$ for the jig shape
$\mathbf{K}_{M\Delta}$	$\mathbf{K}_M$ for the deflected geometry
$\mathbf{K}_S$	Stiffness matrix for the structural equations
L/D	Lift-to-drag ratio of the aircraft
$\mathscr{L}$	Lagrangian function
l, u	Lower and upper bound for an inequality constraint
m	Number of mesh movement increments
m_J	m used in mesh movement for the jig shape
m_Δ	m used in mesh movement for the deflected geometry
$\mathscr{N}$	B-spline basis functions
$\hat{N}$	Number of B-spline control points in each direction
N_e	Number of elements in the structural model
n_{eq}, n_{in}	Number of equality and inequality constraints
p	Order of the B-spline basis functions
$\mathbf{q}$	Aerodynamic state vector
$\mathbf{r}$	All rigid link vectors
$\mathbf{R}_{AS}$	Aerostructural residual vector
$\mathbf{R}_A$	Aerodynamic residual vector
$\mathbf{R}_{MJ}$	Mesh residual vector for the jig shape
$\mathbf{R}_{M\Delta}$	Mesh residual vector for the deflected shape
$\mathbf{R}_S$	Structural residual vector
T	B-spline knot values
$\mathbf{u}$	Structural state vector
$\mathbf{u}_A$	Changes in the aerodynamic surface coordinates due to structural deflections
$\mathbf{v}$	Design variables
$\mathbf{v}_A$	Aerodynamic design variables
$\mathbf{v}_G$	Geometric design variables
$\mathbf{v}_S$	Structural design variables
W_i	Weight of the aircraft at the beginning of cruise
W_f	W_i minus the fuel weight
W	Weight of the wing
W_0	Initial weight of the wing
$\mathbf{x}$	Coordinates of a point in physical space
β	Scalar parameter between 0 and 1
λ	Load factor in a structural element
ρ	Positive weighting parameter for the Kreisselmeier-Steinhauser function
σ	von Mises stress in a structural element
σ_{yield}	Material yield stress
Ψ_A	Aerodynamic adjoint vector
$\Psi_{M\Delta}$	Mesh adjoint vector corresponding to the flying shape
Ψ_{MJ}	Mesh adjoint vector corresponding to the jig shape
Ψ_S	Structural adjoint vector
θ	Under-relaxation factor
Υ	Parameteric coordinates of a point in space
ξ, η, ζ	Individual parametric coordinates

1 Introduction

Future-generation aircraft must be substantially more fuel efficient to sustain rapid growth of the aviation industry with increasing environmental concern for greenhouse gas emissions. Conventional tube-and-wing designs are highly optimized and offer limited room for further improvements. Unconventional design options must be explored to achieve the required amount of efficiency gain (Torenbeek and Deconinck, 2005). This poses a challenge with the traditional cut-and-try approach to aircraft design because it relies heavily on the knowledge and experience of the designer that is not always available for unconventional configurations. This challenge is being gradually overcome with numerical optimization based on high-fidelity aerodynamic analysis. Although computationally more expensive than low-fidelity models, high-fidelity aerodynamic analysis accurately captures the physics of the flow under conditions where low-fidelity models can be inaccurate.

This work is motivated by the desire to perform high-fidelity exploratory aerostructural optimization where the optimizer is given as much geometric freedom as possible in order to explore a large design space. In this context, it is often not necessary to consider all of the aspects involved in detailed design. Exploratory optimization can require hundreds and sometimes thousands of design variables. This, together with the cost of large-scale high-fidelity calculations, makes gradient-based optimization methods the preferred option. The cost of optimization can be further reduced by the use of adjoint methods, where the cost of gradient calculations is almost independent of the number of design variables (Pironneau, 1974; Jameson, 1988). High-fidelity exploratory optimization is especially valuable when exploring unconventional design concepts, enabling rapid assessment and comparison of competing concepts.

Aerodynamic shape optimization has revealed several promising design concepts that lead to reductions in drag (Hicken and Zingg, 2010b; Gagnon and Zingg, 2016b). What remains an interesting and important question is how much of these benefits are offset by the possible increase in structural weight. Although some recent applications of high-fidelity aerodynamic optimization have included simplified weight models (Leoviriyakit et al, 2004; Jameson et al, 2007; Reist et al, 2013; Lyu and Martins, 2014), the tradeoff between drag and weight is more accurately captured with full stress analysis based on aerodynamic loading. Coupling aerodynamic and structural analysis automatically accounts for the effects of the structural deflections on the aerodynamic performance (Reuther et al, 1999). It also provides more accurate indication of possible structural failure, reducing the reliance on artificial geometric constraints that can steer the optimizer away from finding the most efficient design (Reuther et al, 1999). Hence, optimization based on tightly integrated high-fidelity aerostructural analysis is an important step towards taking full advantage of numerical optimization. Development of such a framework for design exploration of unconventional aircraft is the focus of this paper.

Shape optimization requires a method to parameterize the geometry of interest and a control mechanism to accomplish shape changes. Geometry parameterization refers to the way that the geometry is defined in space. Perhaps the most obvious example is the discrete parameterization technique where the geometry is defined using the individual grid nodes. Other examples include parameterization via analytical shape functions such as those proposed by Hicks and Henne (1978), PARSEC (Sobieczky, 1998), Non-Uniform Rational B-Spline (NURBS) (Piegl and Tiller, 1997), or its variations such as B-spline or Bézier curves (Braibant and Fleury, 1984). In contrast, geometry control more precisely refers to the way shape changes are applied to the geometry during optimization. For instance, a geometry may be parameterized by B-spline surfaces, but controlled with FFD volumes that make changes to the B-spline control points rather than the discrete set of surface grid nodes (Gagnon and Zingg, 2015).

An ideal geometry parameterization describes the geometry with a compact set of design variables, yet at the same time gives the optimizer sufficient flexibility to develop design features of interest to the designer. For gradient-based optimization, the availability of geometric gradients with respect to design variables is an important consideration (Samareh, 2001). CAD, or computer-aided-design, tools are powerful for creating complex geometries in aircraft design (Samareh, 1999). A CAD-based optimization approach uses the CAD software to make changes to the original CAD model. However, the design variable sensitivities of the geometry are often unavailable for at least the two following reasons: proprietary code within the CAD software and a geometry that does not necessarily vary smoothly due to the use of a patch topology (Samareh, 1999; Truong et al, 2016). In contrast, CAD-free methods have been developed that do not involve the use of CAD software. These avoid the above difficulties and also can be much simpler to use than a CAD package because they can be tailored to a specific application. Hence CAD-free methods can be advantageous for exploratory design studies and such a method is presented here.

In the context of aerostructural optimization, shape changes across disciplines must be consistently parameterized to maintain the accuracy of the analysis (Samareh, 2001; Kenway et al, 2010). Additionally, design shape changes cannot be analyzed without efficient and robust mesh movement algorithms to deform the aerodynamic and structural domains. The aerodynamic domain undergoes further deformations during aerostructural analysis due to structural deflections. This stems from the fact that the aerodynamic analysis typically uses an Eulerian formulation (Farhat et al, 1995). An efficient aerodynamic mesh movement algorithm that is capable of handling large geometry changes is hence essential. In contrast, the structural analysis often uses a Lagrangian formulation, so that the structural mesh movement is only executed once per design cycle for changes in the unstressed geometry. Nevertheless, the structural mesh movement should minimize the introduction of any undesirable distortions in the structural members, such as ribs and spars, modeled in high-fidelity analysis.

The above challenges have been addressed in different ways in the existing literature on high-fidelity aerostructural optimization. Farhat *et al.* (1995) proposed a three-field formulation to handle the motion of the flow grid due to structural deflections during transient aerostructural analysis. The flow grid was modeled explicitly alongside the flow and structural equations. This led to three coupled equations in the aeroelastic problem. Maute *et al.* (2001) applied the three-field formulation to aerostructural optimization based on steady analysis involving the Euler equations and a linear structural analysis. The flow grid was modeled based on a spring analogy. During optimization, simple geometry changes to the outer mold line (OML) of a wing as well as the detailed finite-element model of the internal structure were parameterized using a number of Coons elements. The proposed methodology was applied to the optimization of an Aeroelastic Research Wing (ARW2). They used a direct method for gradient calculation. The same authors later described an alternative methodology using a coupled adjoint approach for gradient calculation (Maute et al, 2003). Barcelos *et al.* (2008) expanded on the three-field methodology by modeling the flow with the Navier-Stokes equations and an algebraic turbulence model, and by using a nonlinear analysis of the structures.

Reuther *et al.* (1999) and Martins *et al.* (2004; 2005) used an OML geometry database as an interface to the optimizer and between the disciplines. This allowed for the design of more general aircraft components. The flow grid was moved by an algebraic warping algorithm which did not appear explicitly in the equations of state, resulting in a two-field formulation. Martins *et al.* (2005) further described the corresponding coupled adjoint approach for gradient calculation. In another paper (Martins et al, 2004), the design framework was applied to the optimization of a supersonic business jet based on the Euler equations and a linear finite-element analysis of the structures. Kenway *et al.* (2010) proposed a way to control the OML and the internal structure using a free-form-deformation (FFD) technique. Deformation of the aerodynamic domain was achieved via a hybrid linear elasticity mesh movement. Using the same geometry parameterization and mesh movement methodology, Kenway *et al.* (2014c) addressed the limitations in the work of Martins *et al.* (2005) by coupling a more advanced Euler solver with a fully parallel structural analysis package in a high-fidelity aerostructural optimization framework. Accuracy and efficiency of the gradient calculations were improved. The described framework was used in the optimization of a NASA Common Research Model (CRM) wing-body-tail configuration (Kenway et al, 2014b). In a recent publication, Kenway *et al.* (2014a) conducted aerostructural optimization studies based on the Reynolds-Averaged Navier-Stokes equations with the CRM geometry.

None of the approaches summarized above use three-dimensional B-spline patches for geometry parameterization. This is also the case in a number of other methodologies not discussed above, including that of Abu-Zurayk and Brazillon (2011) and Samareh (2000). Although B-splines have been widely used for shape parameterization in purely aerodynamic and structural optimization (Braibant and Fleury, 1984; Cosentino and Holst, 1986; Schramm and Pilkey, 1993; Anderson and Venkatakrishnan, 1997), they are clearly lacking popularity in the field of fully coupled aerostructural optimization. As Samareh (2001; 2000) pointed out, there are a few significant challenges that have prevented the use of B-splines for aerostructural optimization despite the many advantages they provide for shape parameterization. For instance, it is difficult to generate grids for the flow and structures after geometry changes. Furthermore, the complex three-dimensional models are difficult to create outside of a CAD system. However, the successful application of B-splines for aerodynamic shape optimization suggests that its potential for aerostructural optimization in the context of aircraft design should not be overlooked (Reuther and Jameson, 1995; Bisson and Nadarajah, 2015; Masters et al, 2016). For this reason, the present paper proposes to use the integrated geometry parameterization and mesh movement of Hicken and Zingg (2010a) that was initially presented for purely aerodynamic shape optimization. This integrated approach has been shown to produce high quality flow meshes even for very large geometric changes, thus enabling optimization where the shape can change dramatically during the optimization where other mesh movement algorithms will often fail (Hicken and Zingg, 2010a).

The integrated approach has two key components that distinguish it from existing methodologies for aerostructural optimization: an effective means for geometry parameterization and control using B-splines, and an efficient and robust mesh movement strategy. Both are essential in exploratory optimization based on high-fidelity aerostructural analysis. This approach parameterizes the grid for flow calculations by B-spline tensor volumes. B-spline control points on the surface of the geometry simultaneously provide effective geometry parameterization and control. There is no clear winner when it comes to the best geometry parameterization, but there are a number of inherent advantages to using B-spline surfaces. They lead to a compact set of design variables and yet still provide a high degree of flexibility that is crucial for exploratory optimization (Samareh, 2001). B-spline curves of order p are known to lie within the convex hull of p neighbouring control points, and the control points approximate the curves (Rogers and Adams, 1990). This allows for local control of shape changes and intuitive specification of geometric constraints. It also means that the B-spline parameterization has a high surface awareness which can be exploited for additional aerodynamic benefits during optimization (Reuther and Jameson, 1995; Lee, 2015). As a result, B-spline surface control points have worked well as geometric design variables (Hicken and Zingg, 2010b; Reist et al, 2013; Osusky et al, 2015), i.e. for both parameterization and control. The physical relationship between the surface control points and the underlying geometry has also allowed them to be used as part of a two-level FFD approach (Gagnon and Zingg, 2015), where the geometry control is provided by FFD volumes. Furthermore, the approximation power of piecewise smooth B-spline surface patches allows complex geometries to be analytically represented and maintained throughout optimization. The initial and optimized geometries are therefore always independent of the mesh used to approximate them. The analytical geometry description may also be used for other important purposes such as rigorous mesh refinement studies, solution-adaptive gridding during the solution process, and high-order mesh generation (Hughes et al, 2005; Persson and Peraire, 2009; Yano et al, 2011). Finally, Hicken and Zingg (2010a) were the first to tightly integrate the geometry parameterization via B-splines to a linear elasticity mesh movement of the B-spline control volumes. This offers a novel way to reduce the cost to the traditional linear-elasticity mesh movement of the actual computational grid while maintaining grid quality. Nevertheless, it is sufficiently robust to preserve the grid quality in the presence of large shape changes, as will be illustrated in Section 6.1. For the above reasons, the integrated geometry parameterization and mesh movement algorithm is particularly well-suited for geometry parameterization and control for optimization with large geometry changes.

The integrated geometry parameterization and mesh movement technique has been successfully applied to aerodynamic shape optimization of a wide range of aircraft configurations involving substantial geometry changes (Hicken and Zingg, 2010b; Gagnon and Zingg, 2015, 2016a,b).The objective of the present paper is to extend this approach to aerostructural optimization. The original integrated approach by Hicken and Zingg (2010a) addressed the challenges associated with creating the B-spline model and the computational fluid dynamics (CFD) grid generation, as pointed out by Samareh (2000; 2001). The main contribution of this paper lies in overcoming two additional challenges. First, a new algorithm must be introduced to move the internal structure consistently with the B-spline geometry. This is accomplished in Section 3.3 by a surface-based FFD method. Second, it must also be shown that the B-spline mesh movement presents a feasible alternative to existing methodologies in accounting for shape changes due to structural deflections, in addition to those due to optimization. Section 4 accomplishes this by adopting a three-field formulation, where the mesh equations are in terms of the B-spline control grid coordinates instead of the flow grid coordinates. This results in a much smaller mesh problem, which is another advantage to using the integrated approach for aerostructural optimization. Finally, the gradient is calculated using an augmented coupled adjoint approach, as discussed in Section 5. The results presented in Section 6.1 have been carefully chosen to demonstrate the robustness of the mesh movement scheme for analysis and optimization. Section 6.2 illustrates the ability of the methodology to capture the correct aerostructural trends. Finally, the test case presented in Section 6.3 is specifically designed to demonstrate the integrated approach in the context of an aerostructural optimization problem with large geometry changes.

2 Aerostructural Optimization Problem Overview

An aerostructural optimization problem involves the minimization of an objective function, $\mathscr{J}$, with respect to a set of design variables, $\mathbf{v}$. The optimization is subject to a partial differential equation constraint, namely the discrete steady aerostructural equations, $\mathbf{R}_{AS}$. The optimization may also be subject to a number of equality constraints, $\mathscr{C}_{\text{eq}}$, and inequality constraints, $\mathscr{C}_{\text{in}}$, which may be linear or nonlinear. The optimization problem can be summarized as follows:

$$\begin{aligned}
&\min_{\mathbf{v}} && \mathscr{J}(\mathbf{v}, [\mathbf{q},\mathbf{u},\mathbf{b}_\Delta]^T)\,, && \quad (1)\\
&\text{subject to:} && \mathbf{R}_{AS}(\mathbf{v}, [\mathbf{q},\mathbf{u},\mathbf{b}_\Delta]^T) = 0\,, &&\\
& && \mathscr{C}_{\text{eq},i}(\mathbf{v}, [\mathbf{q},\mathbf{u},\mathbf{b}_\Delta]^T) = 0\,, && i = 1,\cdots,n_{\text{eq}}\\
& l_j \le && \mathscr{C}_{\text{in},j}(\mathbf{v}, [\mathbf{q},\mathbf{u},\mathbf{b}_\Delta]^T) \le u_j\,, && j = 1,\cdots,n_{\text{in}}
\end{aligned}$$

The lower and upper bounds for the j^{th} inequality constraint are given by l_j and u_j, respectively. The aerostructural state variables are given by $[\mathbf{q},\mathbf{u},\mathbf{b}_\Delta]^T$, where $\mathbf{q}$ is the flow state, $\mathbf{u}$ is the structural state, and $\mathbf{b}_\Delta$ is the state of the aerodynamic grid with structural deflections. By solving $\mathbf{R}_{AS}(\mathbf{v}, [\mathbf{q},\mathbf{u},\mathbf{b}_\Delta]^T) = 0$, the state variables become a function of $\mathbf{v}$. The optimization problem is solved using SNOPT (Gill et al, 1997; Perez et al, 2012), which is a third-party gradient-based optimization package that is well-suited for large-scale, nonlinear optimization problems.

Aerostructural analysis allows multidisciplinary objectives, including both aerodynamic and structural functionals, to be evaluated and minimized. Examples of objective functions include range, fuel burn, or some linear combination of weight and drag for more specific tradeoff studies. A lift constraint specified in terms of the weight of the aircraft is often necessary. To avoid structural failure, a Kreisselmeier-Steinhauser (KS) aggregation function (Wrenn, 1989; Akgün et al, 1999; Kennedy and Martins, 2010) is used to ensure that the von Mises stress values of all structural elements are below the yield stress of the material by a specified factor of safety. Constraints on the geometry may also be included. The design variables are categorized into geometric (i.e. $\mathbf{v}_G$), aerodynamic (i.e. $\mathbf{v}_A$), and structural (i.e. $\mathbf{v}_S$) design variables. For this work, aerodynamic design variables consist of an angle of attack for each load condition. Structural design variables specify the thickness of individual structural members. To capture the important tradeoff between weight and drag, the main load bearing components of a wingbox are modeled, including spars, ribs, top skin, and bottom skin. This paper uses the coordinates of the surface B-spline control points as geometric design variables, as will be discussed in Section 3.

Structural constraints such as flutter and buckling are not currently considered. However, the purpose of this work is not to accurately capture all realistic aspects of practical aircraft design, but to explore methodologies which can effectively capture the important tradeoffs between weight and drag, while enabling substantial geometric variation. Steady-state aerostructural analysis, with structural sizing based on the von Mises failure criterion, is sufficient for this purpose, and it will serve as an important step towards incorporating unsteady and dynamic effects in the future.

3 Integrated Geometry Parameterization and Mesh Movement

3.1 Geometry and Flow Grid Parameterization using B-Spline Surfaces and Volumes

The integrated geometry parameterization and mesh movement technique uses a B-spline tensor-product volume which maps a point from parametric space, $D = \{\Upsilon = (\xi,\eta,\zeta) \in \mathbb{R}^3 | \xi,\eta,\zeta \in [0,1]\}$, to physical space, $P \subset \mathbb{R}^3$, according to the following mathematical relationship

$$\mathbf{x}(\Upsilon) = \sum_{i=1}^{\hat{N}_i} \sum_{j=1}^{\hat{N}_j} \sum_{k=1}^{\hat{N}_k} \mathbf{B}_{ijk} \mathscr{N}_i^{(p)}(\xi) \mathscr{N}_j^{(p)}(\eta) \mathscr{N}_k^{(p)}(\zeta)\,, \qquad (2)$$

where $\mathbf{B}_{ijk}$ are the coordinates of the de Boor control points, and $\mathscr{N}_i^{(p)}(\xi)$, $\mathscr{N}_j^{(p)}(\eta)$, $\mathscr{N}_k^{(p)}(\zeta)$ are B-spline basis functions of order p in each parametric coordinate direction. The grid of B-spline control points embeds and fully describes the computational grid for flow calculations, given the parametric coordinates of all flow grid nodes in the control volume. The flow grid can be modified via changes to the B-spline control volume, and the number of control grid nodes is typically about two orders of magnitude fewer than the number of flow grid nodes. Describing the state of the flow grid in terms of B-spline control points also reduces the size of the analysis and adjoint problems.

Hicken and Zingg (2010a) used generalized basis functions that incorporate spatially varying knots, so that they can be tailored to different edges of a geometry. Basis functions in the $\xi-$direction are given by

$$\mathcal{N}_i^{(1)}(\xi;\eta,\zeta) = \begin{cases} 1 \text{ if } T_i(\eta,\zeta) \leq \xi < T_{i+1}(\eta,\zeta) \\ 0 \text{ otherwise} \end{cases} \tag{3}$$

$$\mathcal{N}_i^{(p)}(\xi;\eta,\zeta) = \left(\frac{\xi - T_i(\eta,\zeta)}{T_{i+p-1}(\eta,\zeta) - T_i}\right)\mathcal{N}_i^{(p-1)}(\xi;\eta,\zeta) + \left(\frac{T_{i+p}(\eta,\zeta) - \xi}{T_{i+p}(\eta,\zeta) - T_{i+1}(\eta,\zeta)}\right)\mathcal{N}_{i+1}^{(p-1)}(\xi;\eta,\zeta),$$

where $T_i(\eta,\zeta)$ are the knot values. Open knot vectors are used. The first and last p knots of $T_i(\eta,\zeta)$ are forced to be 0 and 1, respectively, and the internal knots follow a bilinear distribution. The basis functions $\mathcal{N}_j^{(p)}(\eta;\xi,\zeta)$ and $\mathcal{N}_k^{(p)}(\zeta;\xi,\eta)$ are defined similarly.

To create the B-spline volume, parametric coordinates of each node in the initial flow grid are determined using a chord-length parameterization. A chord-length-based knot distribution is obtained by placing an equal number of nodes within each knot interval. The B-spline control point coordinates are found by a least-squares fitting of the flow grid. The control volume has mesh spacing that resembles a coarsened flow grid due to the nature of the knot distribution. This characteristic is exploited in the flow grid movement. For the multi-block structured grids used in this work, each block is represented by a separate control grid with coincident control points at the block interfaces to ensure continuity (Hicken and Zingg, 2010a).

Control points at the surface of the geometry define a set of B-spline surface patches which analytically describe the geometry of interest. This naturally leads to an effective geometry parameterization, where a wide range of geometries can be specified by the optimizer via moving the surface control points. During aerostructural analysis, surface control points additionally describe the flying shape. Therefore, coordinates of the surface control points, $\mathbf{b}_s$, are functions of $\mathbf{v}_G$ and $\mathbf{u}$.

3.2 Flow Grid Movement

Changes in the B-spline surfaces are propagated to the interior of the control volume via a linear elasticity mesh movement algorithm. Large shape changes are broken into m increments. Given $\mathbf{b}_s^{(i)}$, which define the force vector, $\mathbf{f}_M^{(i)}$, the vector of control point coordinates, $\mathbf{b}^{(i)}$, is updated by solving, for $i = 1,\cdots,m$ (Hicken and Zingg, 2010a):

$$\mathbf{R}_M^{(i)}(\mathbf{b}^{(i-1)},\mathbf{b}^{(i)}) = \mathbf{K}_M^{(i)}(\mathbf{b}^{(i-1)})[\mathbf{b}^{(i)} - \mathbf{b}^{(i-1)}] - \mathbf{f}_M^{(i)}(\mathbf{b}_s^{(i)}) = 0 \tag{4}$$

where $\mathbf{R}_M^{(i)}$ is the mesh residual and $\mathbf{K}_M^{(i)}$ the stiffness matrix. A spatially-varying Young's modulus is used to preserve the quality of the control grid, which makes $\mathbf{K}_M^{(i)}$ a function of $\mathbf{b}^{(i-1)}$. For clarity, $\mathbf{b}_s^{(i)}$ is not a subset of $\mathbf{b}^{(i)}$, but rather an input to (4) that is determined according to

$$\mathbf{b}_s^{(i)} = \frac{i}{m}\left(\mathbf{b}_s^{(m)} - \mathbf{b}_s^{(0)}\right) + \mathbf{b}_s^{(0)}, \quad i = 1,\cdots,m. \tag{5}$$

The difference given by $(\mathbf{b}_s^{(m)} - \mathbf{b}_s^{(0)})$ is the total displacement of the B-spline surface control points. The solution of (4) is found by the parallel preconditioned conjugate-gradient (PCG) solver from the PETSc library (Balay et al, 1997). The new flow grid is simply re-evaluated according to (2). To simplify the notation from this point on, $\mathbf{R}_M$ refers to the vector containing all the incremental mesh residuals, i.e. $\mathbf{R}_M = [\mathbf{R}_M^{(1)},\mathbf{R}_M^{(2)},\cdots,\mathbf{R}_M^{(m)}]^T$. A similar notation is used for $\mathbf{b}$ and $\mathbf{b}_s$. Linear elasticity mesh movement is very robust in the presence of large shape changes. It is also much cheaper to apply this method to the control grid instead of the flow grid. The quality of the flow grid is nonetheless preserved by the similarity in the mesh spacing between the control grid and the flow grid.

In aerostructural optimization, changes in the geometry are the combined result of changes due to optimization and structural deflections. Changes due to optimization are measured from the initial geometry and are independent of the aerostructural analysis. A balance between robustness and efficiency is achieved by moving the grid in two sets of increments. The grid for the jig shape is obtained by solving (4) before an analysis, using m_J increments with $\mathbf{b}^{(0)}$ set to that of the initial control grid. The reason is that using a consistent $\mathbf{b}^{(0)}$ between all design iterations is necessary to ensure the smoothness of the gradient. Equation (4) is then coupled to the aerostructural analysis using another m_Δ increments to obtain the grid for the deflected geometry, with $\mathbf{b}^{(0)}$ set to $\mathbf{b}^{(m_J)}$. Hence mesh movement during analysis only needs to accommodate shape changes due to structural deflections. This allows for a relatively small m_Δ that is independent of the larger m_J, that might be needed to reflect the often larger changes in the jig shape. Grid quality is then ensured without incurring a significant cost penalty in the aerostructural calculations. This is particularly essential in exploratory optimization where significant shape changes are likely to occur. The subscripts $_J$ and $_\Delta$ are used to distinguish between the mesh equations and variables for the jig shape and the deflected shape.

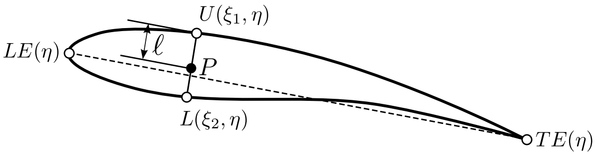

Fig. 1: The straight line which associates a structural mesh node, P, with the surfaces of a wing section described by a constant spanwise parametric coordinate η.

3.3 Structural Mesh Movement

The structural model remains fixed during aerostructural analysis, but shape changes described by the B-spline surfaces must be translated consistently to the structural model for accurate force and displacement transfer. Despite the flexibility offered by B-spline surfaces, FFD provides a simpler and more effective way to move the structural model because it is geometric fidelity independent (Sederberg and Parry, 1986; Kenway et al, 2010). A surface-based FFD method is hence developed which parameterizes the space enclosed by the B-spline surfaces and allows it to act as an FFD volume in moving the structures. This method is suitable for any geometry with a well-defined leading and trailing edge in the B-spline surface parameterization, and is sufficient for many aerostructural design applications. It can be modified to handle more general geometries.

Given a point P on the structural model, the surface-based FFD method begins by associating it with two points U and L, on the upper and lower surfaces of the geometry, respectively. This is illustrated in Figure 1. The coordinates of U and L are given by

$$\begin{aligned} U(\xi_1,\eta) &= \sum_{j=1}^{\hat{N}_j}\sum_{k=1}^{\hat{N}_k}\mathcal{N}_j(\xi_1)\mathcal{N}_k(\eta)\mathbf{B}_{jk\hat{N}_m}\,, \\ L(\xi_2,\eta) &= \sum_{j=1}^{\hat{N}_j}\sum_{k=1}^{\hat{N}_k}\mathcal{N}_j(\xi_2)\mathcal{N}_k(\eta)\mathbf{B}_{jk1}\,, \end{aligned} \tag{6}$$

where ξ_1, ξ_2 and η are the chordwise and spanwise parametric coordinates of U and L on the B-spline surfaces, and $\mathbf{B}_{jk\hat{N}_m}$ and $\mathbf{B}_{jk1}$ are the corresponding surface control points. The points P, U, and L are collinear so that the coordinates of P can be described by a parametric distance ℓ as follows:

$$U(\xi_1,\eta)+\ell\,[L(\xi_2,\eta)-U(\xi_1,\eta)]-P=0\,. \tag{7}$$

The appropriate U and L are found for each P at the start of an optimization. The values of ξ_1, ξ_2, η and ℓ are then fixed for the remainder of the optimization, and the coordinates of P become a function of the B-spline surface control points. Since U and L share the same η, P will always remain in the same spanwise section traced by a constant η. In order to associate each P with a unique pair of (U,L), two constraints are defined based on vector dot products:

$$\text{Let: } \begin{cases} \overrightarrow{UP} &= U(\xi_1,\eta)-P \\ \overrightarrow{LP} &= L(\xi_2,\eta)-P \\ \overrightarrow{C} &= TE(\eta)-LE(\eta) \end{cases} \text{, then: } \begin{cases} \overrightarrow{UP}\cdot\overrightarrow{C} &= 0 \\ \overrightarrow{LP}\cdot\overrightarrow{C} &= 0 \end{cases}. \tag{8}$$

Equation (8) requires that the line UPL (see Figure 1), along which P is parameterized, to be normal to the chord defined by the leading edge, LE, and trailing edge, TE, of the same η. For most structural layouts, this ensures that UPL is close to being tangent to the ribs and spars and is aligned with the direction in which sectional shape changes are defined. This can reduce the amount of unwanted distortions introduced to the structural components during shape changes. The surface-based FFD method effectively defines an FFD control volume directly from the B-spline surfaces, but it imposes few restrictions on the number and distribution of control points on the upper and lower surfaces.

The surface-based FFD approach can be applied to most geometries that are relevant to the static aerostructural design of an aircraft. For future extensions to more complex geometries, such as a split-tip wing where a straight line through U, P and L may not exist for all P, the search of U and L is programmed as a minimization problem solved by SQP (Nocedal and Wright, 2006). The cost of associating all points on the structural model with the B-spline geometry definition is negligible in comparison to the aerostructural optimization. Re-evaluation of the new structural geometry involves simple algebraic expressions and is extremely efficient. Geometric sensitivities of the structural mesh points with respect to the surface control points can be easily obtained using the chain rule.

4 Steady-State Aerostructural Analysis

The present methodology adopts a three-field formulation of the discrete steady aerostructural equations. The mesh equations, $\mathbf{R}_{M\Delta}$, appear explicitly in the aerostructural residual, $\mathbf{R}_{AS}$, along with the aerodynamic equations, $\mathbf{R}_A$, and the structural equations, $\mathbf{R}_S$:

$$\mathbf{R}_{AS}=\begin{bmatrix}\mathbf{R}_A(\mathbf{q},\mathbf{b}_\Delta)\\ \mathbf{R}_S(\mathbf{q},\mathbf{u},\mathbf{b}_\Delta)\\ \mathbf{R}_{M\Delta}(\mathbf{u},\mathbf{b}_\Delta)\end{bmatrix}=0\,. \tag{9}$$

A two-field formulation of $\mathbf{R}_{AS}$, which consists only of the aerodynamic and structural equations, treats the flow grid as an intermediate variable. This leads to an explicit dependence of $\mathbf{R}_A$ on $\mathbf{u}$, or $\partial\mathbf{R}_A/\partial\mathbf{u}\neq 0$. It can be recovered from (9) by solving $\mathbf{R}_{M\Delta}=0$ for every change in $\mathbf{u}$. Evaluating $\partial\mathbf{R}_A/\partial\mathbf{u}$ also requires the partial derivative of the flow grid, $\mathbf{G}$, with respect to $\mathbf{u}$. However, this term cannot be easily obtained for the present mesh movement strategy because the mesh nodes are implicitly coupled to $\mathbf{u}$ via the surface control points according to (4). It is therefore more efficient and straightforward to use a three-field formulation.

The present aerostructural framework is constructed over existing aerodynamic, structural and mesh movement modules. The solution to (9) is obtained via a nonlinear block Gauss-Seidel method, which involves sub-iterations using existing solution routines within each module. Results obtained by aerostructural analysis are validated with experimental data from the HIRENASD project, as shown in Appendix A.

4.1 Aerodynamic Analysis

The Euler equations governing compressible inviscid flow are discretized on the multi-block structured mesh using second-order summation-by-parts finite-difference operators (Hicken and Zingg, 2008). The use of simultaneous-approximation terms simplifies interface solution coupling and boundary treatments, while maintaining solution accuracy and time stability. The discrete steady aerodynamic equations are written as

$$\mathbf{R}_A(\mathbf{q}, \mathbf{b}_\Delta) = 0\,. \tag{10}$$

Equation (10) has an explicit dependence on $\mathbf{G}$, which is in turn a function of $\mathbf{b}_\Delta$. Given $\mathbf{b}_\Delta$, (10) is solved for $\mathbf{q}$ by an efficient parallel implicit Newton-Krylov-Schur algorithm.

4.2 Structural Analysis

The structural analysis is provided by the Toolkit for the Analysis of Composite Structures (TACS) (Kennedy and Martins, 2014a,b). The present work assumes a linear constitutive relationship, and geometric nonlinearity is not considered. The structural components are modeled using second-order mixed interpolation of tensorial components (MITC) shell elements (Dvorkin and Bathe, 1984), resulting in the following equations:

$$\mathbf{R}_S(\mathbf{q}, \mathbf{u}, \mathbf{b}_\Delta) = \mathbf{K}_S\mathbf{u} - \mathbf{f}_S(\mathbf{q}, \mathbf{b}_\Delta) = 0\,. \tag{11}$$

The force vector, $\mathbf{f}_S$, in this case is a result of aerodynamic loading, the magnitude and direction of which are explicit functions of $\mathbf{q}$ and $\mathbf{b}_\Delta$. Given $\mathbf{f}_S$, (11) is solved by GMRES preconditioned by a direct Schur method.

TACS also calculates the structural mass and stress constraint. The stress constraint requires the load factor, λ_k, in every element k, to satisfy $\lambda_k = \mathrm{FoS} \times (\sigma_k/\sigma_{\mathrm{yield}}) \leq 1$, where σ_k is the von Mises stress in the element, σ_{yield} is the yield stress of the material, and FoS is a factor of safety. The number of constraints is reduced by aggregating the failure criteria from groups of elements using a Kreisselmeier-Steinhauser (KS) function (Wrenn, 1989; Akgün et al, 1999; Kennedy and Martins, 2010), so that gradient calculation using the coupled adjoint method remains efficient. With $\lambda_{\min} = \min\{\lambda_k\}$, the KS function is given by:

$$\mathrm{KS} = \lambda_{\min} - \frac{1}{\rho} \ln \left\{ \sum_{k=1}^{N_e} \exp\left[-\rho(\lambda_k - \lambda_{\min})\right] \right\}, \tag{12}$$

where N_e is the number of elements and ρ is a positive weighting parameter specified by the user.

4.3 Force and Displacement Transfer

The aerodynamic, structural, and mesh equations are coupled by the transfer of forces and displacements at the aerostructural interface. The interface includes flow grid nodes on the parts of the geometry which are not assumed rigid, and structural nodes adjacent to the aerodynamic surface. The present framework uses a rigid link method in TACS (Kennedy and Martins, 2014a). The rigid link vectors are created at the start of optimization, where each flow grid node at the interface is paired with the closest point on the structural model. This allows displacements and forces to be extrapolated between the aerodynamic and structural grids, which may not necessarily overlap at the interface.

The rigid link method translates $\mathbf{u}$ into a vector of displacements, $\mathbf{u}_A$, for all nodes at the surface of the flow grid. The mesh movement, however, requires the displacement of the B-spline surfaces. A discrete set of coordinates, $\tilde{\mathbf{G}}_{s\Delta}$, on the deflected geometry is first obtained by adding $\mathbf{u}_A$ to $\mathbf{G}_{sJ}$, which is a vector of surface grid nodes on the jig shape. A new set of B-spline surfaces that best describes the deflected geometry is then found by least-squares fitting. Due to the error in fitting, surface grid coordinates described by the B-spline surfaces may not be the same as those in $\tilde{\mathbf{G}}_{s\Delta}$. Some possible implications of this error on the accuracy of the analysis have been investigated by Zhang *et al.* (2015). It has been shown that the error in displacement transfer as introduced by the fitting does not affect the grid convergence of important functionals. On the other hand, the grid smoothing introduced by the fitting can improve the convergence of the analysis in some cases. Whether or not the fitting is desirable hence deserves further investigation.

4.4 Nonlinear Block Gauss-Seidel Iterations

Prior to an aerostructural analysis, the flow grid for the jig shape is obtained by solving $\mathbf{R}_{MJ}$ given $\mathbf{b}_{sJ}(\mathbf{v}_G)$, and the structures are moved according to Section 3.3. The appropriate freestream conditions are assigned according to $\mathbf{v}_A$. Structural stiffness is evaluated according to $\mathbf{v}_S$ and the updated structural geometry. Equation (9) is solved via a nonlinear block Gauss-Seidel method. Aitken acceleration (Irons and Tuck, 1969; Küttler and Wall, 2008) is used to improve the stability and convergence of the analysis. The relative tolerance for the aerostructural problem is typically set to 10^{-7}.

The nonlinear block Gauss-Seidel method allows the flow, mesh, and structural modules to be integrated in a straightforward manner. Nonetheless, they may suffer from efficiency and stability issues for strongly coupled problems. More effective monolithic methods have been proposed in the literature to address such issues (Heil et al, 2008; Tezduyar and Sathe, 2007; Bazilevs et al, 2008). The development of more advanced solution strategies for the present work is currently underway.

5 Gradient Calculation by the Coupled Adjoint Method

The coupled adjoint formulation has been previously described by various authors (Martins et al, 2005; Maute et al, 2001). It is presented here for the current aerostructural optimization methodology, using the method of Lagrange multipliers adopted by Hicken and Zingg (2010a) for aerodynamic optimization. Consider the optimization of a functional $\mathscr{J}$, subject to $\mathbf{R}_{AS}=0$ and $\mathbf{R}_{MJ}=0$. The Lagrangian function for this problem is

$$\begin{aligned}\mathscr{L} = {} & \mathscr{J}(\mathbf{v},\mathbf{b}_J,[\mathbf{q},\mathbf{u},\mathbf{b}_\Delta]^T)+\Psi_{MJ}^T\mathbf{R}_{MJ}(\mathbf{v},\mathbf{b}_J) \\ & + \left[\Psi_A^T\ \Psi_S^T\ \Psi_{M\Delta}^T\right]\begin{bmatrix}\mathbf{R}_A(\mathbf{v},\mathbf{b}_J,[\mathbf{q},\mathbf{b}_\Delta]^T)\\ \mathbf{R}_S(\mathbf{v},\mathbf{b}_J,[\mathbf{q},\mathbf{u},\mathbf{b}_\Delta]^T)\\ \mathbf{R}_{M\Delta}(\mathbf{v},\mathbf{b}_J,[\mathbf{u},\mathbf{b}_\Delta]^T)\end{bmatrix},\end{aligned} \tag{13}$$

where Ψ_{MJ}, Ψ_A, Ψ_S and $\Psi_{M\Delta}$ are the Lagrange multipliers. Square brackets are used around $\mathbf{R}_{AS}=[\mathbf{R}_A,\mathbf{R}_S,\mathbf{R}_{M\Delta}]^T$ and $[\mathbf{q},\mathbf{u},\mathbf{b}_\Delta]^T$ to indicate that they are fully coupled as a single term. The first-order optimality conditions require that the partial derivatives of $\mathscr{L}$ with respect to $\mathbf{b}_J$ and $[\mathbf{q},\mathbf{u},\mathbf{b}_\Delta]^T$ be zero:

$$\begin{aligned}&\frac{\partial\mathscr{L}}{\partial\mathbf{b}_J}=0 \quad \Rightarrow \\ &\Psi_{MJ}^T\frac{\partial\mathbf{R}_{MJ}}{\partial\mathbf{b}_J}+\left[\Psi_A^T\Psi_S^T\Psi_{M\Delta}^T\right]\left(\frac{\partial}{\partial\mathbf{b}_J}\begin{bmatrix}\mathbf{R}_A\\ \mathbf{R}_S\\ \mathbf{R}_{M\Delta}\end{bmatrix}\right)=-\frac{\partial\mathscr{J}}{\partial\mathbf{b}_J}, \\ &\frac{\partial\mathscr{L}}{\partial[\mathbf{q},\mathbf{u},\mathbf{b}_\Delta]^T}=0 \quad \Rightarrow \\ &\left[\Psi_A^T\Psi_S^T\Psi_{M\Delta}^T\right]\left(\frac{\partial}{\partial[\mathbf{q},\mathbf{u},\mathbf{b}_\Delta]^T}\begin{bmatrix}\mathbf{R}_A\\ \mathbf{R}_S\\ \mathbf{R}_{M\Delta}\end{bmatrix}\right)=-\frac{\partial\mathscr{J}}{\partial[\mathbf{q},\mathbf{u},\mathbf{b}_\Delta]^T}.\end{aligned} \tag{14}$$

Taking the transpose of the above equations leads to

$$\left[\begin{array}{c|ccc}\frac{\partial\mathbf{R}_{MJ}}{\partial\mathbf{b}_J}^T & 0 & 0 & \frac{\partial\mathbf{R}_{M\Delta}}{\partial\mathbf{b}_J}^T \\ \hline & \frac{\partial\mathbf{R}_A}{\partial\mathbf{q}}^T & \frac{\partial\mathbf{R}_S}{\partial\mathbf{q}}^T & 0 \\ 0 & 0 & \frac{\partial\mathbf{R}_S}{\partial\mathbf{u}}^T & \frac{\partial\mathbf{R}_{M\Delta}}{\partial\mathbf{u}}^T \\ & \frac{\partial\mathbf{R}_A}{\partial\mathbf{b}_\Delta}^T & \frac{\partial\mathbf{R}_S}{\partial\mathbf{b}_\Delta}^T & \frac{\partial\mathbf{R}_{M\Delta}}{\partial\mathbf{b}_\Delta}^T\end{array}\right]\left[\begin{array}{c}\Psi_{MJ}\\ \hline \Psi_A\\ \Psi_S\\ \Psi_{M\Delta}\end{array}\right]=\left[\begin{array}{c}0\\ \hline -\frac{\partial\mathscr{J}}{\partial\mathbf{q}}^T\\ -\frac{\partial\mathscr{J}}{\partial\mathbf{u}}^T\\ -\frac{\partial\mathscr{J}}{\partial\mathbf{b}_\Delta}^T\end{array}\right]. \tag{15}$$

The derivation is completed by taking the partial derivative of $\mathscr{L}$ with respect to $\mathbf{v}$:

$$\begin{aligned}\mathscr{G}= {} & \frac{\partial\mathscr{J}}{\partial\mathbf{v}}^T+\frac{\partial\mathbf{R}_{MJ}}{\partial\mathbf{v}}^T\Psi_{MJ} \\ & +\left(\frac{\partial\mathbf{R}_A}{\partial\mathbf{v}}^T\Psi_A+\frac{\partial\mathbf{R}_S}{\partial\mathbf{v}}^T\Psi_S+\frac{\partial\mathbf{R}_{M\Delta}}{\partial\mathbf{v}}^T\Psi_{M\Delta}\right),\end{aligned} \tag{16}$$

which is the expression for the total gradient of $\mathscr{J}$ with respect to the design variables. The Lagrange multipliers here are the adjoint variables. The coupled adjoint equations refer to the block 3×3 system in (15), where $[\Psi_A,\Psi_S,\Psi_{M\Delta}]^T$ are coupled by the transposed Jacobian of $\mathbf{R}_{AS}$ on the left-hand side. The coupled adjoint problem is augmented by the mesh adjoint equations for the jig shape in the first row of (15). Gradient evaluation involves first solving (15) for all adjoint variables, and subsequently evaluating (16).

Calculation of the partial derivative terms follows the work of Kenway *et al.* (2014c), but appropriate modifications have been introduced for the three-field formulation adopted here. To facilitate further discussion on the gradient calculation, it is convenient to distinguish between aerodynamic functionals, $\mathscr{J}_A$, and structural functionals, $\mathscr{J}_S$. Aerodynamic functionals, such as lift and drag, have no explicit dependence on structural variables. Conversely, structural functionals, such as mass and the KS functions, have no explicit dependence on aerodynamic variables. Composite functionals of interest in this work can be written in terms of pure aerodynamic and structural functionals.

The coupled adjoint problem in (15) is solved via a linear block Gauss-Seidel method. Each iteration solves the following equations in sequence:

$$\frac{\partial\mathbf{R}_A}{\partial\mathbf{q}}^T\Psi_A^{(k+1)}=-\frac{\partial\mathscr{J}}{\partial\mathbf{q}}^T-\frac{\partial\mathbf{R}_S}{\partial\mathbf{q}}^T\Psi_S^{(k)} \tag{17}$$

$$\mathbf{K}_S\Psi_S^{(k+1)}=-\frac{\partial\mathscr{J}}{\partial\mathbf{u}}^T-\frac{\partial\mathbf{R}_{M\Delta}}{\partial\mathbf{u}}^T\Psi_{M\Delta}^{(k)} \tag{18}$$

$$\frac{\partial\mathbf{R}_{M\Delta}}{\partial\mathbf{b}_\Delta}^T\Psi_{M\Delta}^{(k+1)}=-\frac{\partial\mathscr{J}}{\partial\mathbf{b}_\Delta}^T-\frac{\partial\mathbf{R}_A}{\partial\mathbf{b}_\Delta}^T\Psi_A^{(k+1)}-\frac{\partial\mathbf{R}_S}{\partial\mathbf{b}_\Delta}^T\Psi_S^{(k+1)}, \tag{19}$$

where k is the iteration number. The iterations are repeated until the residual norms of all equations drop below a specified tolerance relative to their initial values.

The flow adjoint equation in (17) is not significantly modified from the two-field formulation described in Kenway *et al.* (2014c). The term $(\partial \mathbf{f}_A/\partial \mathbf{q})^T$, as needed for $(\partial \mathbf{R}_S/\partial \mathbf{q})^T \Psi_S$, is analytically differentiated for the present framework. Equation (17) is solved by a flexible variant of GCROT preconditioned in the same manner as the flow equations (Hicken and Zingg, 2010a). The transposed flow Jacobian, $(\partial \mathbf{R}_A/\partial \mathbf{q})^T$, is computed by a combination of analytical and complex-step differentiation, and stored.

With a three-field formulation, the aerodynamic forces are explicit functions of $\mathbf{b}_\Delta$ instead of $\mathbf{u}$. For this reason, $(\partial \mathscr{I}_A/\partial \mathbf{u})^T$ is zero in (18). Similarly, contributions of the following forces in the structural Jacobian, i.e. $(\partial \mathbf{f}_S/\partial \mathbf{u})^T(\partial \mathbf{R}_S/\partial \mathbf{f}_S)^T \Psi_S^{(k)}$, are also zero. The effects of $\mathbf{u}$ on the mesh movement are included in

$$\frac{\partial \mathbf{R}_{M\Delta}}{\partial \mathbf{u}}^T \Psi_{M\Delta} = \frac{\partial \mathbf{u}_A}{\partial \mathbf{u}}^T \frac{\partial \tilde{\mathbf{G}}_{s\Delta}}{\partial \mathbf{u}_A}^T \frac{\partial \mathbf{b}_{s\Delta}}{\partial \tilde{\mathbf{G}}_{s\Delta}}^T \frac{\partial \mathbf{R}_{M\Delta}}{\partial \mathbf{b}_{s\Delta}}^T \Psi_{M\Delta}\,, \tag{20}$$

where all terms are differentiated analytically. In particular, $(\partial \mathbf{b}_{s\Delta}/\partial \tilde{\mathbf{G}}_{s\Delta})^T$ is obtained by differentiating the linear least-squares surface fitting. The last term, $(\partial \mathbf{u}_A/\partial \mathbf{u})^T$ is computed in TACS (Kennedy and Martins, 2014a). Equation (18) is solved by the same routines as in structural analysis due to the symmetry of $\mathbf{K}_S$.

In the mesh adjoint equation in (19), $(\partial \mathscr{I}_S/\partial \mathbf{b}_\Delta)^T$ is zero. Furthermore, $(\partial \mathscr{I}_A/\partial \mathbf{b}_\Delta)^T$ and $(\partial \mathbf{R}_A/\partial \mathbf{b}_\Delta)^T \Psi_A$ are obtained by differentiating with respect to the flow grid, $\mathbf{G}$, then completing the chain rule by $(\partial \mathbf{G}/\partial \mathbf{b}_\Delta)^T$ from the B-spline volume definition. The term $(\partial \mathbf{R}_S/\partial \mathbf{b}_\Delta)^T \Psi_S$ accounts for the contribution of $\mathbf{G}$, as a function of $\mathbf{b}_\Delta$, in the surface traction calculation and in the force transfer (Kennedy and Martins, 2014a), and is analytically differentiated. All partial derivative terms on the right-hand side of (19) are only non-zero with respect to $\mathbf{b}_\Delta^{(m_\Delta)}$. Hence (19) is solved as the following m_Δ equations:

For $i = m_\Delta$: (21)

$$\left(\frac{\partial \mathbf{R}_{M\Delta}^{(m_\Delta)}}{\partial \mathbf{b}_\Delta^{(m_\Delta)}}\right)^T \Psi_{M\Delta}^{(m_\Delta)} = -\frac{\partial \mathscr{I}}{\partial \mathbf{b}_\Delta^{(m_\Delta)}}^T - \frac{\partial \mathbf{R}_A}{\partial \mathbf{b}_\Delta^{(m_\Delta)}}^T \Psi_A - \frac{\partial \mathbf{R}_S}{\partial \mathbf{b}_\Delta^{(m_\Delta)}}^T \Psi_S\,,$$

For $i = m_\Delta - 1, \cdots, 1$:

$$\left(\frac{\partial \mathbf{R}_{M\Delta}^{(i)}}{\partial \mathbf{b}_\Delta^{(i)}}\right)^T \Psi_{M\Delta}^{(i)} = -\left(\frac{\partial \mathbf{R}_{M\Delta}^{(i+1)}}{\partial \mathbf{b}_\Delta^{(i)}}\right)^T \Psi_{M\Delta}^{(i+1)}\,,$$

where each equation is solved by the parallel PCG solver in PETSc (Balay et al, 1997).

After solving the coupled adjoint problem, the mesh adjoint equation for the jig shape is solved for Ψ_{MJ}. Control grid coordinates for the jig shape, $\mathbf{b}_J$, only appear in $\mathbf{R}_{M\Delta}$. The jig shape mesh adjoint equation is hence reduced to

$$\frac{\partial \mathbf{R}_{MJ}}{\partial \mathbf{b}_J}^T \Psi_{MJ} = -\frac{\partial \mathbf{R}_{M\Delta}}{\partial \mathbf{b}_J}^T \Psi_{M\Delta}\,. \tag{22}$$

More specifically, $\mathbf{b}_J^{(m_J)}$ is involved in the calculation of the stiffness, $\mathbf{K}_{M\Delta}$, and the implicit force vector, $\mathbf{f}_{M\Delta}$, in $\mathbf{R}_{M\Delta}$. Equation (22) then translates to the following m_J equations:

For $i = m_J$: (23)

$$\left(\frac{\partial \mathbf{R}_{MJ}^{(m_J)}}{\partial \mathbf{b}_J^{(m_J)}}\right)^T \Psi_{MJ}^{(m_J)} = -\left(\left.\frac{\partial \mathbf{R}_{M\Delta}^{(1)}}{\partial \mathbf{b}_J^{(m_J)}}\right|_{\mathbf{f}_{M\Delta}^{(1)}}\right)^T \Psi_{M\Delta}^{(1)} + \sum_{j=1}^{m_\Delta}\left(\frac{\partial \mathbf{f}_{M\Delta}^{(j)}}{\partial \mathbf{b}_J^{(m_J)}}\right)^T \Psi_{M\Delta}^{(j)}\,,$$

For $i = m_J - 1, \cdots, 1$:

$$\left(\frac{\partial \mathbf{R}_{MJ}^{(i)}}{\partial \mathbf{b}_J^{(i)}}\right)^T \Psi_{MJ}^{(i)} = -\left(\frac{\partial \mathbf{R}_{MJ}^{(i+1)}}{\partial \mathbf{b}_J^{(i)}}\right)^T \Psi_{MJ}^{(i+1)}\,,$$

which are solved in a similar fashion as (19).

Equation (16) can be simplified for aerodynamic and structural design variables as follows:

$$\mathscr{G}_A = \frac{\partial \mathscr{I}}{\partial \mathbf{v}_A}^T + \frac{\partial \mathbf{R}_A}{\partial \mathbf{v}_A}^T \Psi_A\,, \tag{24}$$

$$\mathscr{G}_S = \frac{\partial \mathscr{I}}{\partial \mathbf{v}_S}^T + \frac{\partial \mathbf{R}_S}{\partial \mathbf{v}_S}^T \Psi_S\,.$$

Gradients with respect to geometric design variables, $\mathbf{v}_G$, are computed differently for the augmented coupled adjoint approach here from other two- and three-field formulations ((Martins et al, 2005; Kenway et al, 2014c; Kennedy and Martins, 2014a; Maute et al, 2003). The terms $(\partial \mathbf{R}_A/\partial \mathbf{v}_G)^T \Psi_A$ and $(\partial \mathscr{I}_A/\partial \mathbf{v}_G)^T$ are both zero. The grid dependence of $\mathbf{R}_A$ and $\mathscr{I}_A$ is instead expressed through the two mesh adjoint terms in (16), where

$$\frac{\partial \mathbf{R}_{MJ}}{\partial \mathbf{v}_G}^T \Psi_{MJ} = \frac{\partial \mathbf{b}_{sJ}}{\partial \mathbf{v}_G}^T \frac{\partial \mathbf{R}_{MJ}}{\partial \mathbf{b}_{sJ}}^T \Psi_{MJ}\,, \tag{25}$$

$$\frac{\partial \mathbf{R}_{M\Delta}}{\partial \mathbf{v}_G}^T \Psi_{M\Delta} = \frac{\partial \tilde{\mathbf{G}}_{s\Delta}}{\partial \mathbf{v}_G}^T \frac{\partial \mathbf{b}_{s\Delta}}{\partial \tilde{\mathbf{G}}_{s\Delta}}^T \frac{\partial \mathbf{R}_{M\Delta}}{\partial \mathbf{b}_{s\Delta}}^T \Psi_{M\Delta}\,. \tag{26}$$

Equations (25) and (26) differ in that $\mathbf{b}_{sJ}$ is an explicit function of $\mathbf{v}_G$, while $\mathbf{b}_{s\Delta}$ depends on $\mathbf{v}_G$ via fitting the discrete deflected geometry in $\tilde{\mathbf{G}}_{s\Delta}$. Furthermore, evaluation of $(\partial \tilde{\mathbf{G}}_{s\Delta}/\partial \mathbf{v}_G)^T$ accounts for changes in both the jig shape and the rigid link vectors (Kenway et al, 2014c). Both $(\partial \mathbf{R}_S/\partial \mathbf{v}_G)^T \Psi_S$ and $(\partial \mathscr{I}_S/\partial \mathbf{v}_G)^T$ need to account for changes in the structural geometry as a result of shape optimization (Martins et al, 2005; Kennedy and Martins, 2014a).

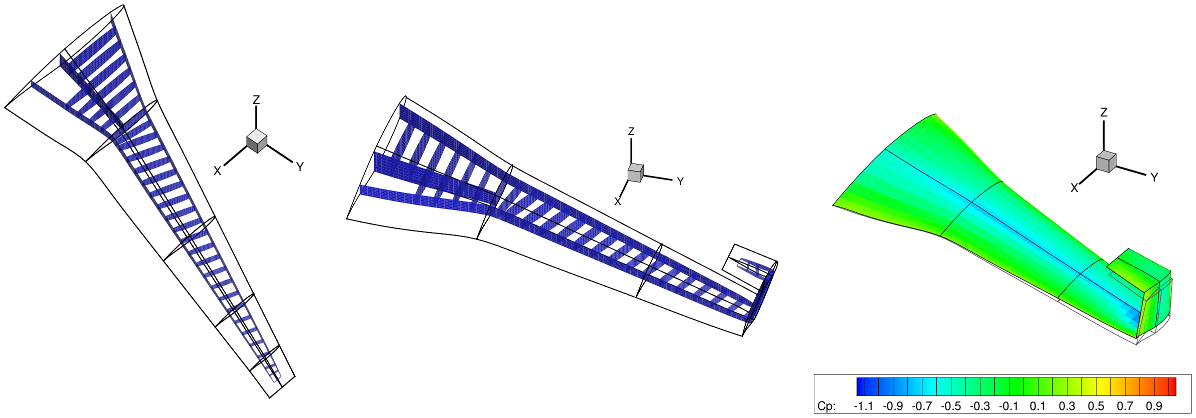

Initial Geometry

New Undeflected Geometry

Deflected Geometry
with Pressure Coefficient, C_p

Fig. 2: Illustration of the ability of the integrated geometry parameterization to handle substantial geometry changes. The right-most figure shows the new geometry and its pressure coefficient contour under structural deflection, which is superimposed on the undeflected geometry.

This involves differentiating (7) for each point on the structural model with respect to $\mathbf{b}_{sJ}$, which is a function of $\mathbf{v}_G$.

Zhang *et al.* (2015) verified the gradient computed using the augmented coupled adjoint approach via comparison with a second-order finite-difference approximation. The majority of the gradient values considered have a minimum relative error on the order of 10^{-8}. This shows that the present methodology is capable of computing accurate gradients.

6 Application to Aerostructural Analysis and Optimization

6.1 Analysis of a C-Wing

To demonstrate the capability of the integrated geometry parameterization and mesh movement to handle large shape changes, a planar wing geometry is manually deformed into a user-specified C-wing geometry using the integrated methodology, and aerostructural analysis based on the Euler equations is performed on the resulting geometry. Although the optimization studies in the subsequent sections also involve large geometry changes, this is a more extreme example that presents a particularly challenging mesh movement problem in both the flow and structure grids. The initial and new undeflected geometries are shown in Figure 2 and have the RAE 2822 airfoil. The aerodynamic grid consists of 193,536 nodes and 112 blocks. Each block is parameterized by $6 \times 6 \times 6$ control points. The surface geometry consists of 20 surface patches, which leads to 30 surface control points in the spanwise direction and 12 in the chordwise direction. The structural model has 30,473 second-order MITC shell elements; it is shown in blue with the initial geometry and the undeflected C-wing. It is evident that the surface-based FFD successfully moved the internal structure without distorting the individual components.

The aerostructural analysis of the C-wing uses a Mach number of 0.785 at an AoA of 0.0° and assumes an altitude of 35,000 feet. The material used for the structures is based on the 7075 Aluminum with a Poisson's ratio of 0.33 and Young's modulus of 70GPa. All structural components in the wing have a thickness of 7.5mm. These parameters are chosen to induce a realistic structural deflection in the wing, which is observed in the final geometry shown on the right in Figure 2.

6.2 Inviscid Transonic Wing Sweep Optimization

There is a fundamental tradeoff between weight and drag in the design of aircraft wings. For instance, at transonic speeds, increasing the quarter-chord sweep angle of a wing reduces the wave drag, but the corresponding increase in the weight may overshadow the drag benefit in such a way that the resulting range is reduced. The main objective of this section is to investigate whether the current framework is able to capture this important tradeoff correctly in the context of an aerostructural optimization of a conventional planar wing.

The choice of the objective function in optimization influences the final optimized design. In the practical design of aircraft wings, the objective is carefully chosen based on the design requirements for a particular aircraft. However, for the purpose of this study, only the tradeoff between weight and drag is of interest. For this reason, the objective function has the form

$$\mathscr{J} = \beta \frac{D}{D_0} + (1-\beta)\frac{W}{W_0}, \tag{27}$$

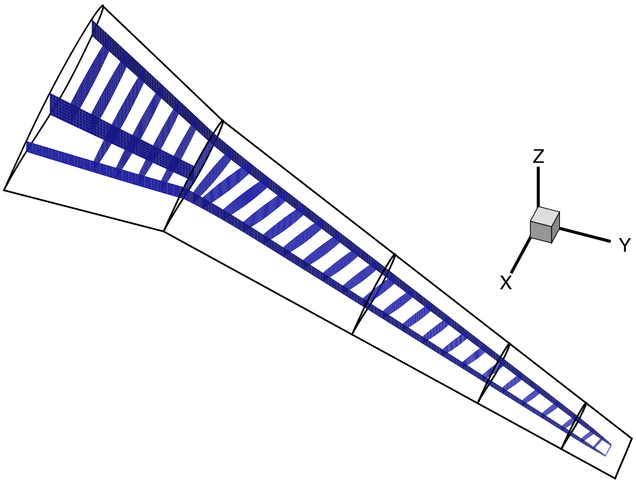

Fig. 3: The outer mold line of the initial wing with the structural components inside the wingbox.

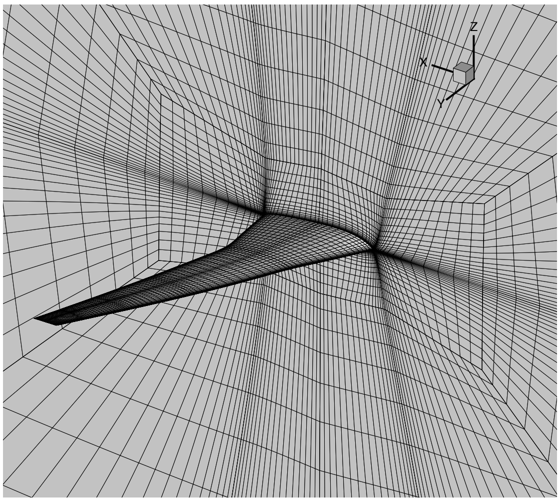

Fig. 4: Grid resolution of the surface and symmetry plane for the fine optimization mesh.

where β is a parameter between zero and unity, D is the inviscid drag of the wing in cruise, W is the calculated weight of the wing satisfying the structural failure constraints at a $2.5g$ load condition, and D_0 and W_0 are the respective initial values. As β is varied from zero to unity, the emphasis on drag in the objective function is increased while reducing the emphasis on weight. Three values for β have been chosen: 0.50, 0.75, and 1.00.

There are two lift constraints; one corresponds to the cruise load condition, the other to the $2.5g$ load condition. The cruise Mach number is 0.785 at an altitude of $35,000$ feet, while the Mach number for the $2.5g$ load condition is 0.798 at an altitude of $12,000$ feet. Since the weight of the wing is a function of the structural thickness values, it changes over the course of the optimization. The total weight of the aircraft is assumed to be equal to the computed weight of the wing plus a fixed weight of $785,000$N. This fixed weight is estimated based on the maximum takeoff weight of a Boeing 737-900 discounted by the approximate wing weight. The approximate wing weight is equal to 7% of the maximum takeoff weight.

The stresses on the wing due to the aerodynamic loads at the $2.5g$ load condition are aggregated using three KS functions with an aggregation parameter of 30.0. There is one KS function for the ribs and spars, one for the top skin, and one for the bottom skin of the wing. These KS functions are constrained to ensure structural integrity of the wing. The material is based on the 7075 Aluminum with a Poisson's ratio of 0.33 and Young's modulus of 70GPa. The yield stress is 434MPa, and a safety factor of two is applied. The reduction in the thickness-to-chord ratio of the wing is limited to 10% of the initial value.

The aerostructural optimizations are initiated with a planar wing geometry based on the Boeing 737-900 planform. Figure 3 shows the layout of the wing and the structures inside the wingbox. Initially, a coarse CFD grid is used with $193,536$ nodes and 112 blocks. Once the optimizer satisfies the nonlinear constraints on this coarse mesh, the optimization is restarted using a finer mesh with $653,184$ nodes and 112 blocks. Figure 4 shows the grid resolution of the surface and symmetry plane for the fine mesh. Each block is parameterized with $6\times6\times6$ control points. The upper and lower surfaces of the wing are parameterized with 10 B-spline surface patches. The structures mesh has $30,473$ second-order MITC shell elements.

The initial airfoil is the RAE 2822. The optimizer is free to change the tip twist and section shape at 16 spanwise stations in addition to the quarter-chord sweep angle. Each spanwise station is parameterized by 24 control points, 14 of which are design variables. The remaining 10 control points are fixed to ensure curvature continuity on the surface of the wing. The sweep angle is varied in such a way that the initial span of the wing is maintained. The total number of geometric design variables is equal to 226. Furthermore, there are a total of 156 structural design variables which determine the thickness of structural components inside the wingbox. Finally, there are two angle of attack design variables; one for cruise, the other for the $2.5g$ load condition.

As β is varied from 0.5 to 1.0, i.e. as more emphasis is placed on drag and less on weight, the optimizer should take advantage of the available freedom to increase the sweep angle of the wing in order to reduce drag. As a result, the sweep angles of the optimized designs should increase with increasing β. Figure 5 shows the planform of the three optimized wings. The wing with $\beta = 1.0$ has a 16% lower drag and a 49% higher weight than the wing with $\beta = 0.5$. It is clear that the optimizer has produced the expected trend. This demonstrates that the present aerostructural optimiza-

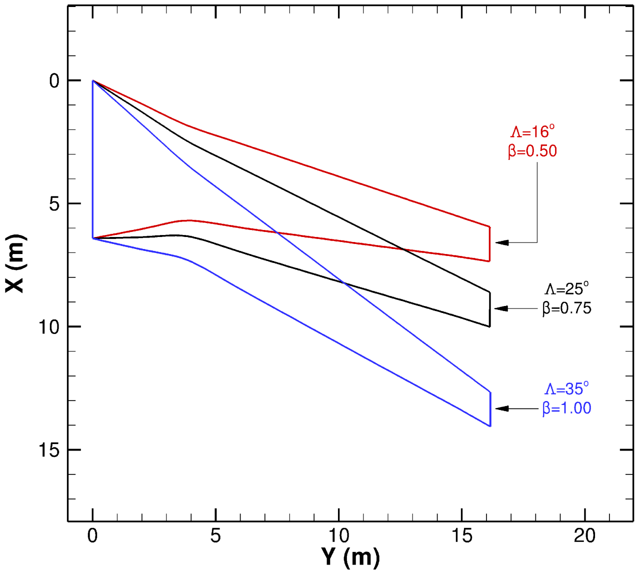

Fig. 5: The planforms for the three wings show that the optimal sweep angle, Λ, increases with increasing β, i.e. increasing emphasis on drag.

tion framework is capable of capturing the tradeoff between weight and drag.

Figures 6 and 7 show the spanwise lift distributions at the cruise and 2.5g load conditions for the $\beta = 1.0$ and $\beta = 0.5$ cases, respectively. All lift values have been normalized by the elliptical lift at the root of the wing for cruise. For the $\beta = 1.0$ case, the cruise lift distribution closely follows the elliptical load, while the 2.5g spanwise lift distribution is much more triangular in comparison to cruise. This means that the optimizer is taking advantage of aeroelastic tailoring to minimize inviscid drag in cruise both by maintaining an optimal lift distribution and increasing the quarter-chord sweep angle. This is done while maintaining the structural integrity of the wing at the 2.5g load condition by reducing the tip loading. It is also insightful to examine the $\beta = 0.5$ case. With $\beta = 0.5$, the lift distributions for both the cruise and 2.5g load conditions are triangular because the objective function is more heavily biased towards the weight of the wing.

Figures 8 and 9 show the optimized skin thickness distribution for the $\beta = 0.5$ and $\beta = 1.0$ cases, respectively. The optimizer has increased the thickness inboard in both cases. Furthermore, it is clear that the $\beta = 0.5$ case has lighter components in comparison to the $\beta = 1.0$ case. Although only a single critical structural load condition has been considered, these results show that at least some of the correct trends in the structural sizing of a wing have been captured.

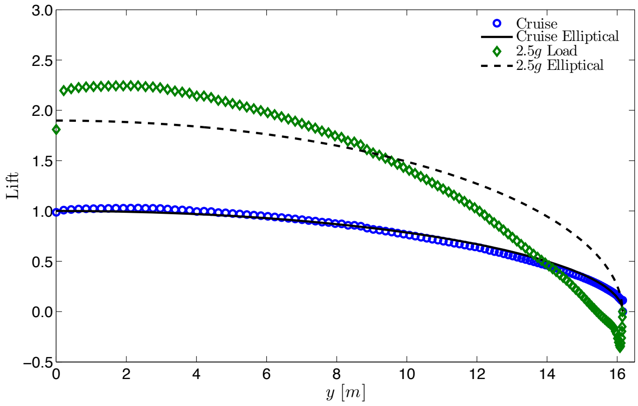

Fig. 6: Cruise and 2.5g load distributions along the span of the wing for the $\beta = 1.0$ case.

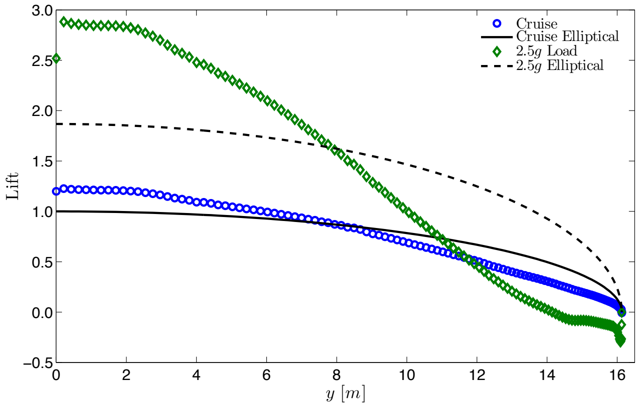

Fig. 7: Cruise and 2.5g load distributions along the span of the wing for the $\beta = 0.5$ case.

6.3 Exploratory Aerostructural Optimization

This section demonstrates the ability of the proposed aerostructural analysis and optimization methodology to perform exploratory optimization with large geometric variation. The planform of the initial wing is based on the Boeing 737-900 aircraft with the RAE 2822 supercritical airfoil. Figure 10 shows the planform of the initial geometry along with the structural layout. Two load conditions are considered: cruise and a 2.5g load case to size the structures. The Mach number at the cruise condition is equal to 0.785 at an altitude of 35,000 feet, while the Mach number for the 2.5g load condition is equal to 0.798 at an altitude of 12,000 feet.

The choice of the objective function for optimization has important implications on the characteristics of the final optimal design. In practical design of aircraft, the objective function is chosen based on a wide range of operational considerations in addition to the mission requirements of the airplane. However, our main goal here is to demonstrate the capability of the proposed methodology for conducting exploratory design optimization. As a result, an objective func-

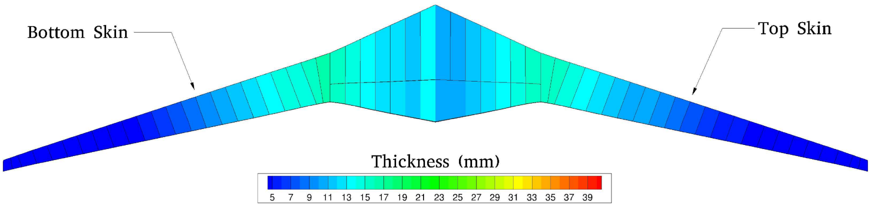

Fig. 8 The optimized thickness distribution of skin elements for the $\beta = 0.5$ case.

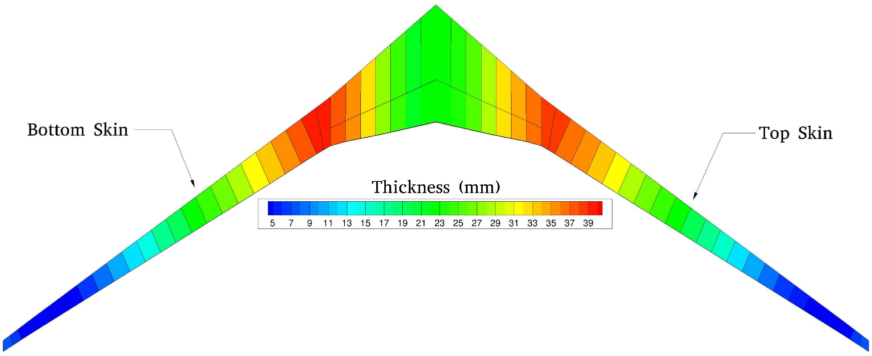

Fig. 9 The optimized thickness distribution of skin elements for the $\beta = 1.0$ case.

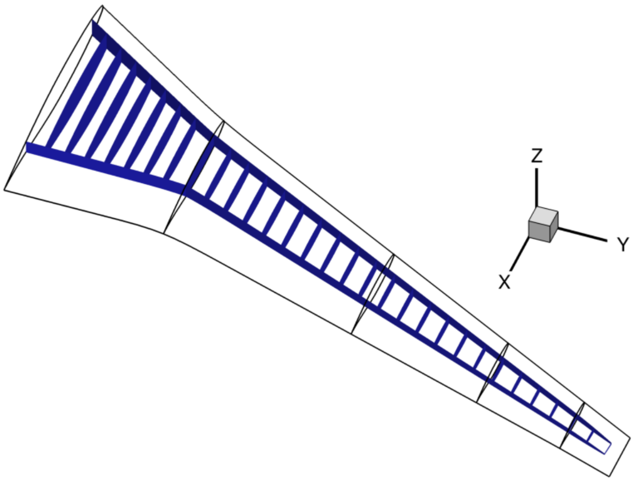

Fig. 10: The outer mold line of the initial wing for the drooped-wing case with the ribs and spars.

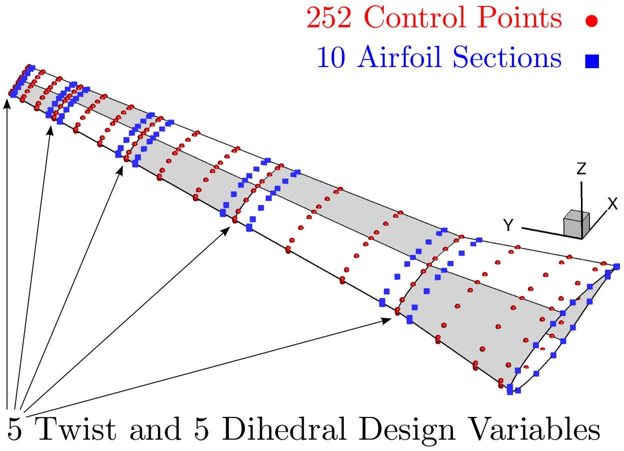

Fig. 11: Geometric parameterization and design variables for the drooped-wing case.

tion of the form

$$\mathscr{J} = -\frac{L}{D}\log\frac{W_i}{W_f} \tag{28}$$

is chosen, where L/D is the inviscid lift-to-drag ratio of the wing, W_i is the initial weight, and W_f is W_i minus the fuel weight. The fuel mass is estimated to be around 21,000kg. This objective function serves as a surrogate for the Breguet range formulation since the cruise speed and the specific fuel consumption are assumed to be fixed. The initial weight of the aircraft is assumed to be equal to the weight of the wing plus a fixed weight of 785,000N. The weight of the wing is calculated by multiplying the weight obtained from the finite-element model by a factor of 1.5 to account for the weight of the load-bearing members that are not included in the structural finite-element model of the wing (Kennedy and Martins, 2014a).

Figure 11 shows the geometric parameterization and design variables used in this optimization case. The upper and lower surfaces of the wing are each broken into 5 regions. The optimizer is free to change the twist and dihedral angle of each region. In addition, the z-coordinates of the B-spline control points are allowed to vary at 10 spanwise stations indicated by blue cubes in Figure 11. The airfoil shapes are interpolated between every pair of control point stations in such a way that slope continuity is maintained along the sur-

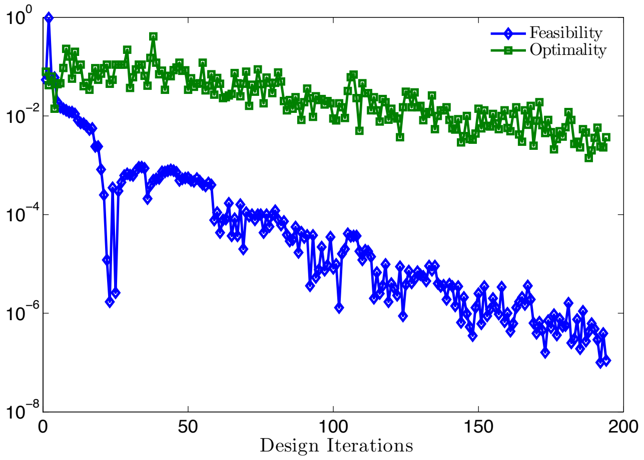

Fig. 12: Convergence of optimality and feasibility for the drooped-wing case.

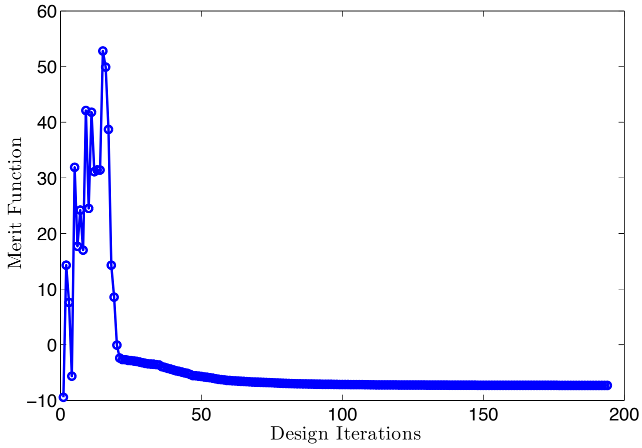

Fig. 13: Convergence of the merit function for the drooped-wing case.

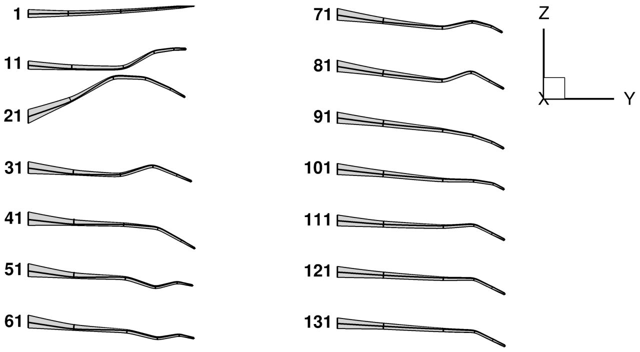

Fig. 14: Functional evaluation number along with back-view of the wing shapes analyzed during optimization. The shapes correspond to the deflected state at the cruise condition.

face of the wing. The projected span of the undeflected wing is constrained to its initial value. There are 150 structural design variables describing the thickness of the structural components, and two angle of attack design variables for the two load conditions.

There are two lift constraints: one for cruise and one for the $2.5g$ load condition. At each load condition, there are three KS constraints to ensure the structural integrity of the ribs and spars, top skin, and bottom skin of the wing. This allows the optimizer to capture some of the important effects of structural sizing on the aerodynamic performance of the wing.

Due to the broad range of geometric freedom given to the optimizer, this case is particularly challenging in terms of optimization convergence. To mitigate some of these challenges, the optimization is performed in two stages. The first stage uses a coarse aerodynamic grid with $149,072$ nodes. Once the optimizer satisfies the nonlinear constraints, the optimization is continued on the finer mesh with $458,752$ nodes. The finite-element model of the structures has $30,030$ second-order MITC shell elements.

Figures 12 and 13 show the convergence history for this optimization case. Feasibility is a measure of the highest nonlinear constraint violation, and optimality is a measure of the gradient of the objective function and constraints. The merit function approaches the objective function value when the feasibility measure is small. These figures indicate that the optimization has reached an acceptable level of convergence. Figure 14 shows the evolution of the wing geometry over the course of optimization. It demonstrates that the optimizer is able to assess a wide variety of unconventional shapes during optimization, and the optimization converges to a drooped-wing concept. The final design is able to satisfy all nonlinear constraints to a tight tolerance while providing an objective function improvement of approximately 4% in comparison to an optimal planar wing of the same projected span.

7 Conclusions and Future Work

This paper describes and characterizes the application of the integrated geometry parameterization and mesh movement algorithm of Hicken and Zingg (2010a) to high-fidelity aerostructural optimization problems. This approach analytically describes both the undeflected geometry and the flying shape of the design using B-spline surface control points. It has several advantages as a geometry parameterization and control technique. The geometry parameterization enables, and is tightly integrated with, an efficient and robust mesh movement algorithm that allows high quality computational grids to be obtained for the aerodynamic domain in response to large shape changes. The present paper demonstrates that the integrated geometry parameterization and mesh movement strategy can be successfully extended to aerostructural optimization, and is suitable for use in optimization with large shape changes. This is achieved by introducing a novel structural mesh movement strategy also capable of handling large shape changes. A three-field formulation has also been adopted to simplify the analysis and the coupled adjoint problem, where B-spline control point coordinates are treated as explicit state variables. Details on the aerostructural solution procedure and the coupled adjoint calculations specific to the new methodology have been provided.

Three examples are included to show how the present framework performs in aerostructural applications. The first case is the analysis of a C-wing that is manually generated from a planar wing using the integrated geometry parameterization and mesh movement methodology. This has demonstrated the robustness of the framework in the presence of aggressive shape changes. The framework is also applied in a wing sweep optimization study involving a realistic number of design variables. The results of this study accurately reflect the fundamental tradeoff between weight and drag in aerostructural design problems. Finally, the ability of the proposed methodology to perform exploratory optimization is demonstrated by the application of the framework to a case with a high degree of geometric freedom, producing a novel drooped-wing.

Future development will include the application of the present framework to more practical design problems and exploratory optimization studies. The gradient calculation will be extended to incorporate aerostructural RANS analysis. More efficient and robust aerostructural solution strategies, such as monolithic methods, will be sought to further improve the effectiveness of this framework as a tool for design and exploratory optimization.

Acknowledgements The authors would like to acknowledge Prof. J. R. R. A. Martins at the University of Michigan, Ann Arbor for sharing his framework for the purpose of constructing our methodology. The authors are also grateful for the funding provided by Zonta International Amelia Earhart Fellowships, the Ontario Graduate Scholarship, and the National Sciences and Engineering Research Council Postgraduate Scholarship. Computations were performed on the GPC supercomputer at the SciNet HPC Consortium. SciNet is funded by the Canada Foundation for Innovation under the auspices of Compute Canada, the Government of Ontario, Ontario Research fund - Research Excellence, and the University of Toronto.

Appendix A: Validation Based on the HIRENASD Wing

Although the individual components of the aerostructural analysis capability have been separately validated with experimental results, it is also important to compare the static aeroelastic analysis results with experiment. However, it is quite difficult to find a suitable experimental study for validation. Most of the test articles used in relevant experimental studies are structurally too stiff to provide a meaningful way of assessing the deflections. Furthermore, it is a challenge to replicate the exact experimental conditions and test setup in many cases. Nonetheless, the HIgh REynolds Number Aero-Structural Dynamics (HIRENASD) Project does provide some useful static aeroelastic data along with the relevant geometries for validating the framework.

The HIRENASD Project was initiated to provide experimental aeroelastic data for a large transport wing-body configuration (Ballmann et al, 2006, 2008, 2009). This section compares static aeroelastic computational results obtained using the present framework with the HIRENASD experimental data. In order to model the test conditions accurately, the Reynolds-Averaged-Navier-Stokes (RANS) capability of the flow solver has been used here for the purpose of the aerostructural analysis. The main objective is to demonstrate that the correct physics are captured even in the presence of the fitting errors. Furthermore, the results of this section motivate the future extension of the current framework to aerostructural optimization based on the RANS equations.

The test condition Mach number, angle of attack, and Reynolds number are 0.80, 1.5°, and 7.0×10^6, respectively. An aerostructural analysis is performed to obtain the computational results. The one-equation Spalart-Allmaras turbulence model is used to model the turbulent flow in this test case. Osusky and Zingg (2013) provide comprehensive details on implementation, verification, and validation of the RANS flow solver.

The flow grid has $3,548,095$ nodes with an average y^+ value of 0.24. The finite-element model provided by the HIRENASD project contained solid elements. However, the structural solver, TACS, accepts MITC shell elements only. Furthermore, the current structural model does not include the leading and trailing edges. Thus, an effort has been made to ensure that the structural finite-element model used in this analysis represents the original structure of the HIRENASD wing as closely as possible within these constraints. The finite-element model for the structures has approximately $38,000$ second-order MITC shell elements.

Figure 15 provides a comparison of the computational static aerostructural results with the experimental data. The rigid-body results (where there are no structural deflections) are also provided for reference. Figure 15 demonstrates that the static aerostructural results obtained from the present framework consistently show much better agreement with the experimental data than the rigid CFD computations, especially towards the wingtip. Moreover, the computed tip deflection of 12.6 mm is in excellent agreement with the experimental value of 12.5 mm (Chwalowski et al, 2011).

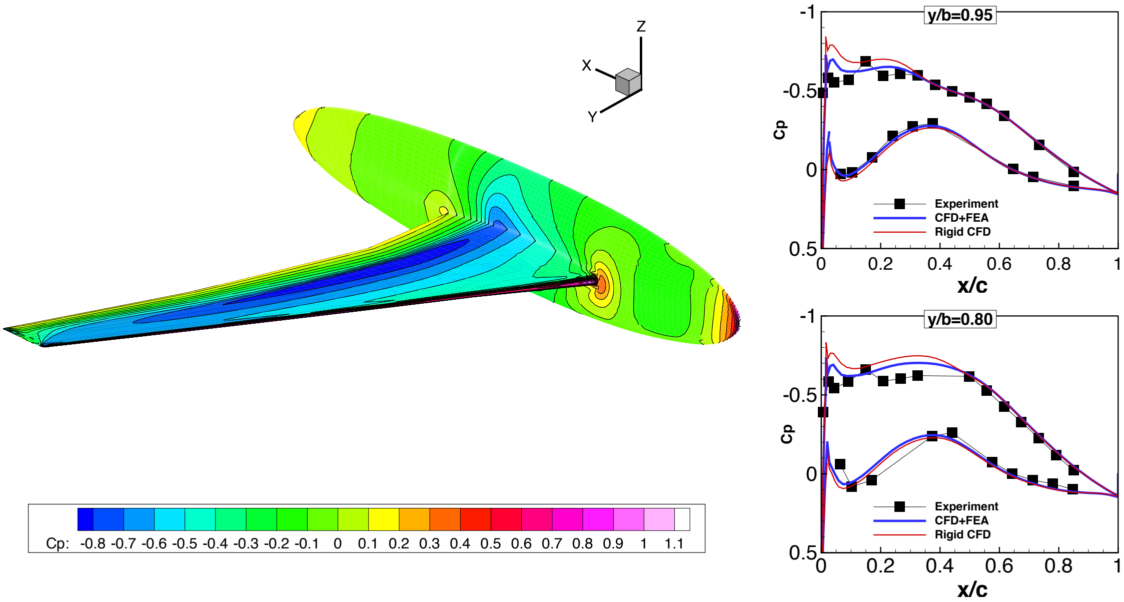

Fig. 15: Comparison of experimental and computational pressure coefficient results for the HIRENASD wing geometry. The experimental (black), static aeroelastic (blue), and rigid-wing results (red) are shown for each spanwise station.

References

Abu-Zurayk M, Brezillon J (2011) Shape optimization using the aerostructural coupled adjoint approach for viscous flows. In: Evolutionary and deterministic methods for design, optimization and control, Capua, Italy

Akgün MA, Haftka RT, Wu KC, Walsh JL (1999) Sensitivity of lumped constraints using the adjoint method. In: 40th Structures, Structural Dynamics, and Materials Conference and Exhibit, St. Louis, Missouri, AIAA-99-1314

Anderson WK, Venkatakrishnan V (1997) Aerodynamic design optimization on unstructured grids with a continuous adjoint formulation. AIAA Paper 97-0643

Balay S, Gropp WD, McInnes LC, Smith BF (1997) Efficient management of parallelism in object oriented numerical software libraries. In: Arge E, Bruaset AM, Langtangen HP (eds) Modern Software Tools in Scientific Computing, Birkhäuser Press, pp 163–202

Ballmann J, Dafnis A, Braun C, Korsch H, Reimerdes HG, Olivier H (2006) The HIRENASD project: High Reynolds number aerostructural dynamics experiments in the European transonic windtunnel (ETW). In: 25th International Congress of the Aeronautical Sciences (ICAS) 2006, Hamburg, Germany, ICAS 2006-10.3.3

Ballmann J, Dafnis A, Korsch H, Buxel C, Reimerdes HG, Brakhage KH, Olivier H, Braun C, Baars A, Boucke A (2008) Experimental analysis of high Reynolds number aero-structural dynamics in ETW. In: 46th AIAA Aerospace Sciences Meeting and Exhibit, Reno, Nevada, AIAA 2008-841

Ballmann J, Boucke A, Dickopp C, Reimer L (2009) Results of dynamic experiments in the HIRENASD project and analysis of observed unsteady processes. In: International Forum on Aeroelasticity and Structural Dynamics (IFASD) 2009, Seattle, Washington, IFASD 2009-103

Barcelos M, Maute K (2008) Aeroelastic design optimization for laminar and turbulent flows. Computer Methods in Applied Mechanics and Engineering 197:1813–1832, DOI 10.1016/j.cma.2007.03.009

Bazilevs Y, Calo VM, Hughes TJR, Zhang Y (2008) Isogeometric fluid-structure interaction: theory, algorithms, and computations. Computational Mechanics 43(1):3–37, DOI 10.1007/s00466-008-0315-x, URL `http://dx.doi.org/10.1007/s00466-008-0315-x`

Bisson F, Nadarajah S (2015) Adjoint-based aerodynamic optimization of benchmark problems. In: 53rd AIAA Aerospace Sciences Meeting, AIAA SciTech, AIAA, AIAA, Kissimmee, FL, aIAA 2015-1948

Braibant V, Fleury C (1984) Shape optimal design using b-splines. Computer Methods in Applied Mechanics and Engineering 44(3):247–267, DOI http://dx.doi.org/10.1016/0045-7825(84)90132-4

Chwalowski P, Florance JP, Heeg J, Wieseman CD (2011) Preliminary computational analysis of the hirenasd configuration in preparation for the aeroelastic prediction workshop. In: International Forum of Aeroelasticity and Structural Dynamics (IFASD), IFASD-2011-108

Cosentino GB, Holst TL (1986) Numerical optimization design of advanced transonic wing configurations. Journal of Aircraft 23(3):193–199

Dvorkin EN, Bathe KJ (1984) A continuum mechanics based four-node shell element for general nonlinear analysis. Engineering Computations 1(1):77–88, DOI 10.1108/eb023562

Farhat C, Lesoinne M, Maman N (1995) Mixed explicit/implicit time integration of coupled aeroelastic problems: Three-field formulation, geometric conservation and distributed solution. International Journal for Numerical Methods in Fluids 21:807–835

Gagnon H, Zingg DW (2015) Two-level free-form and axial deformation for exploratory aerodynamic shape optimization. AIAA Journal 53:2015–2026, DOI 10.2514/1.J053575

Gagnon H, Zingg DW (2016a) Aerodynamic optimization trade study of a box-wing aircraft configuration. Journal of Aircraft 53(4):971–981, DOI http://dx.doi.org/10.2514/1.C033592

Gagnon H, Zingg DW (2016b) Euler-equation-based drag minimization of unconventional aircraft configurations. Journal of Aircraft DOI http://dx.doi.org/10.2514/1.C033591, (Accepted)

Gill PE, Murray W, Saunders MA (1997) SNOPT: An SQP algorithm for large-scale constrained optimization. SIAM Journal on Optimization 12:979–1006

Heil M, Hazel AL, Boyle J (2008) Solvers for large-displacement fluidstructure interaction problems: segregated versus monolithic approaches. Computational Mechanics 43(1):91–101

Hicken JE, Zingg DW (2008) Parallel Newton-Krylov solver for the Euler equations discretized using simultaneous-approximation terms. AIAA Journal 46(11):2773–2786

Hicken JE, Zingg DW (2010a) Aerodynamic optimization algorithm with integrated geometry parameterization and mesh movement. AIAA Journal 48(2):400–413

Hicken JE, Zingg DW (2010b) Induced-drag minimization of nonplanar geometries based on the Euler equations. AIAA Journal 48(11):2564–2575

Hicks RM, Henne PA (1978) Wing design by numerical optimization. Journal of Aircraft 15(7):407–412, DOI 10.2514/3.58379

Hughes TJR, Cottrell JA, Bazilevs Y (2005) Isogeometric analysis: CAD, finite elements, nurbs, exact geometry and mesh refinement. Computer Methods in Applied Mechanics and Engineering 194(39-41):4135–4195, DOI http://dx.doi.org/10.1016/j.cma.2004.10.008

Irons BM, Tuck RC (1969) A version of the Aitken accelerator for computer iteration. International Journal for Numerical Methods in Engineering 1(3):275–277, DOI 10.1002/nme.1620010306, URL http://dx.doi.org/10.1002/nme.1620010306

Jameson A (1988) Aerodynamic design via control theory. Journal of Scientific Computing 3(3):233–260

Jameson A, Leoviriyakit K, , Shankaran S (2007) Multipoint aero-structural optimization of wings including planform variables. In: 45th Aerospace Sciences Meeting and Exhibit, Reno, Nevada, AIAA-2007-0000

Kennedy G, Martins J (2014a) A parallel aerostructural optimization framework for aircraft design studies. Structural and Multidisciplinary Optimization 50(6):1079–1101, DOI 10.1007/s00158-014-1108-9, URL http://dx.doi.org/10.1007/s00158-014-1108-9

Kennedy GJ, Martins JRRA (2010) Parallel solution methods for aerostructural analysis and design optimization. In: 13th AIAA/ISSMO Multidisciplinary Analysis Optimization Conference, Fort Worth, Texas, AIAA-2010-9308

Kennedy GJ, Martins JRRA (2014b) A parallel finite-element framework for large-scale gradient-based design optimization of high-performance structures. Finite Elements in Analysis and Design 87:56–73, DOI 10.1016/j.finel.2014.04.011

Kenway GKW, Kennedy GJ, Martins JRRA (2010) A CAD-free approach to high-fidelity aerostructural optimization. In: Proceedings of the 13th AIAA/ISSMO Multidisciplinary Analysis Optimization Conference, Fort Worth, TX, AIAA 2010-9231

Kenway GKW, Kennedy GJ, Martins JRRA (2014a) Aerostructural optimization of the common research model configuration. In: 15th AIAA/ISSMO Multidisciplinary Analysis and Optimization Conference, Atlanta, GA

Kenway GKW, Kennedy GJ, Martins JRRA (2014b) Multipoint high-fidelity aerostructural optimization of a transport aircraft configuration. Journal of Aircraft 51:144–160, DOI 10.2514/1.C032150

Kenway GKW, Kennedy GJ, Martins JRRA (2014c) Scalable parallel approach for high-fidelity steady-state aeroelastic analysis and adjoint derivative computations. AIAA Journal 52:935–951, DOI 10.2514/1.J052255

Küttler U, Wall WA (2008) Fixed-point fluid–structure interaction solvers with dynamic relaxation. Computational Mechanics 43(1):61–72, DOI 10.1007/s00466-008-0255-5, URL http://dx.doi.org/10.1007/s00466-008-0255-5

Lee C (2015) A comparison of b-spline surface and free-form deformation geometry control methods for aerodynamic shape optimization. Master's thesis, University of Toronto, Toronto

Leoviriyakit K, Kim S, Jameson A (2004) Aero-structural wing planform optimization using the Navier-Stokes equations. In: 10th AIAA/ISSMO Multidisciplinary Analysis and Optimization Conference, Albany, New York, AIAA-2004-4479

Lyu Z, Martins JRRA (2014) Aerodynamic shape optimization studies of a blended-wing-body aircraft. Journal of

Aircraft 51(5):1604–1617, DOI 10.2514/1.C032491

Martins JRRA, Alonso JJ, Reuther JJ (2004) High-fidelity aerostructural design optimization of a supersonic business jet. Journal of Aircraft 41(3):523–530

Martins JRRA, Alonso JJ, Reuther JJ (2005) A coupled-adjoint sensitivity analysis method for high-fidelity aerostructural design. Optimization and Engineering 6:33–62

Masters DA, Poole DJ, Taylor NJ, Rendall T, Allen CB (2016) Impact of shape parameterisation on aerodynamic optimisation of benchmark problem. In: 54th AIAA Aerospace Sciences Meeting, San Diego, CA, 2016-1544

Maute K, Nikbay M, Farhat C (2001) Coupled analytical sensitivity analysis and optimization of three-dimensional nonlinear aeroelastic systems. AIAA Journal 39(11):2051–2061

Maute K, Nikbay M, Farhat C (2003) Sensitivity analysis and design optimization of three-dimensional non-linear aeroelastic systems by the adjoint method. International Journal for Numerical Methods in Engineering 56(6):911–933, DOI 10.1002/nme.599, URL http://dx.doi.org/10.1002/nme.599

Nocedal J, Wright SJ (2006) Numerical Optimization, 2nd edn. Springer, New York

Osusky L, Buckley H, Reist T, Zingg DW (2015) Drag minimization based on the Navier-Stokes equations using a Newton-Krylov approach. AIAA Journal 53(6):1555–1577, DOI 10.2514/1.J053457

Osusky M, Zingg DW (2013) Parallel Newton-Krylov-Schur solver for the Navier-Stokes equations discretized using summation-by-parts operators. AIAA Journal 51(12):2833–2851, DOI 10.2514/1.J052487

Perez RE, Jansen PW, Martins JRRA (2012) pyOpt: A Python-based object-oriented framework for nonlinear constrained optimization. Structures and Multidisciplinary Optimization 45(1):101–118, DOI 10.1007/s00158-011-0666-3

Persson PO, Peraire J (2009) Curved mesh generation and mesh refinement using lagrangian solid mechanics. In: 47th AIAA Aerospace Sciences Meeting including The New Horizons Forum and Aerospace Exposition, Orlando, Florida

Piegl L, Tiller W (1997) The NURBS Book, 2nd edn. Monographs in Visual Communication, Springer-Verlag Berlin Heidelberg, DOI 10.1007/978-3-642-59223-2

Pironneau O (1974) On optimum design in fluid mechanics. Journal of Fluid Mechanics 64(1):97–110

Reist TA, , Zingg DW (2013) Aerodynamic shape optimization of a blended-wing-body regional transport for a short range mission. In: 31st AIAA Applied Aerodynamics Conference, San Diego, CA, 2013-2414

Reuther J, Jameson A (1995) A comparison of design variables for control theory based airfoil optimization. Tech. rep., NASA

Reuther JJ, Alonso JJ, Martins JRRA, Smith SC (1999) A coupled aero-structural optimization method for complete aircraft configurations. In: AIAA 37th Aerospace Sciences Meeting, pp 99–0187

Rogers DF, Adams JA (1990) Mathematical elements for computer graphics. McGraw-Hill, New York

Samareh J (2000) Multidisciplinary aerodynamic-structural shape optimization using deformation (massoud). In: 8th AIAA Symposium on Multidisciplinary Analysis and Optimization, Long Beach, California, 2000-4911

Samareh JA (1999) Status and future of geometry modeling and grid generation for design and optimization. Journal of Aircraft 36(1):97–104, DOI 10.2514/2.2417

Samareh JA (2001) Survey of shape parameterization techniques for high-fidelity multidisciplinary shape optimization. AIAA Journal 39(5):877–884, DOI 0.2514/2.1391

Schramm U, Pilkey WD (1993) Structural shape optimization for the torsion problem using direct integration and b-splines. Computer Methods in Applied Mechanics and Engineering 107(1):251–268

Sederberg TW, Parry SR (1986) Free-form deformation of solid geometric models. In: SIGGRAPH '86 Proceedings of the 13th Annual Conference on Computer Graphics and Interactive Techniques, Dallas, Texas, pp 151–160

Sobieczky H (1998) Flexible wing optimisation based on shapes and structures. In: Fujii K, Dulikravich GS (eds) Recent Development of Aerodynamic Design Methodologies, Notes on Numerical Fluid Mechanics (NNFM), vol 65, Vieweg Verlag, pp 71–88, DOI 10.1007/978-3-322-89952-1_4

Tezduyar TE, Sathe S (2007) Modelling of fluidstructure interactions with the spacetime finite elements: Solution techniques. International Journal for Numerical Methods in Fluids 54(6-8):855–900, DOI 10.1002/fld.1430, URL http://dx.doi.org/10.1002/fld.1430

Torenbeek E, Deconinck H (eds) (2005) Innovative Configurations and Advanced Concepts for Future Civil Aircraft. VKI Lecture Series, von Karman Institute for Fluid Dynamics

Truong A, Zingg DW, Haimes R (2016) Surface Mesh Movement Algorithm for Computer-Aided-Design-Based Aerodynamic Shape Optimization. AIAA Journal 54(2):542–556, DOI 10.2514/1.J054295

Wrenn GA (1989) An indirect method for numerical optimization using the Kreisselmeier–Steinhauser function. Tech. Rep. CR-4220, NASA

Yano M, Modisette J, Darmofal D (2011) The importance of mesh adaptation for higher-order discretizations of aerodynamic flows. In: 20th AIAA Computational Fluid Dynamics Conference, Honolulu, Hawaii, 2011-3852

Zhang ZJ, Khosravi S, Zingg DW (2015) High-fidelity aerostructural optimization with integrated geometry parameterization and mesh movement. In: 56th

AIAA/ASCE/AHS/ASC Structures, Structural Dynamics, and Materials Conference, Kissimmee, FL, 2015-1132